

# Structural and dynamical investigation of glassforming smectogen by X-ray diffraction and infra-red spectroscopy aided by density functional theory calculations

Aleksandra Deptuch<sup>1,\*</sup>, Natalia Górska<sup>2</sup>, Stanisław Baran<sup>3</sup>, Magdalena Urbańska<sup>4</sup>

<sup>1</sup> Institute of Nuclear Physics Polish Academy of Sciences, Radzikowskiego 152, PL-31342 Kraków, Poland

<sup>2</sup> Faculty of Chemistry, Jagiellonian University, Gronostajowa 2, PL-30387 Kraków, Poland

<sup>3</sup> Jagiellonian University, Faculty of Physics, Astronomy and Applied Computer Science, M. Smoluchowski Institute of Physics, Łojasiewicza 11, PL-30-348 Kraków, Poland

<sup>4</sup> Institute of Chemistry, Military University of Technology, Kaliskiego 2, PL-00908 Warsaw, Poland

\*corresponding author, [aleksandra.deptuch@ifj.edu.pl](mailto:aleksandra.deptuch@ifj.edu.pl)

## Abstract

Molecular arrangement in the chiral smectic phases of the glassforming (S)-4'-(1-methylheptylcarbonyl)biphenyl-4-yl 4-[7-(2,2,3,3,4,4,4-heptafluorobutoxy) heptyl-1-oxy]benzoate is investigated by X-ray diffraction. An increased correlation length of the positional short-range order in the supercooled state agrees with the previous assumption of the hexatic smectic phase. However, the registered X-ray diffraction patterns are not typical for the hexatic phases. Comparison of the smectic layer spacing and optical tilt angle indicates a strongly non-linear shape of molecules, which enables choice of the molecular models obtained by DFT calculations, used subsequently to interpret the infra-red spectra. The presumption of the hexatic smectic  $F_A^*$  or  $I_A^*$  phase is supported by the splitting of the absorption bands related to the C=O stretching in the supercooled state, which is absent in the smectic  $C_A^*$  phase above the melting temperature. The glass transition affects the temperature dependence of the smectic layer spacing but only subtly impacts the infra-red spectra. Application of the k-means cluster analysis enables distinction between the infra-red spectra below and above the glass transition temperature, but only for certain spectral ranges.

## 1. Introduction

The family of chiral, partially fluorinated liquid crystalline compounds, with the general formula presented in Figure 1, was introduced in 2008 [1] and extended in 2011 [2] and 2015 [3]. The abbreviation used in this paper is  $mX_1X_2n$ , where  $m$  is the length of the  $C_mH_{2m}$  chain,  $X_1, X_2 = H$  or  $F$  describe the number and position of the fluorine atoms substituted to the benzene ring and  $n$  is the length of the  $C_nH_{2n+1}$  chain. The liquid crystalline phases exhibited by the  $mX_1X_2n$  compounds are the smectic phases characterized by the layer order (Figure 2): paraelectric smectic  $A^*$  ( $SmA^*$ ), ferroelectric  $SmC^*$ , antiferroelectric  $SmC_A^*$  and hexatic  $SmX_A^*$  ( $SmF_A^*$  or  $SmI_A^*$  – they cannot be distinguished based on the available data) [1-6].

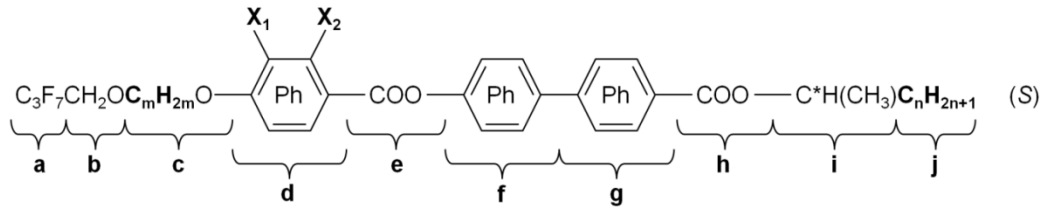


Figure 1. The general molecular formula of the  $mX_1X_2n$  compounds. The notations of the particular fragments of a molecule are used in the description of the intra-molecular vibrations.

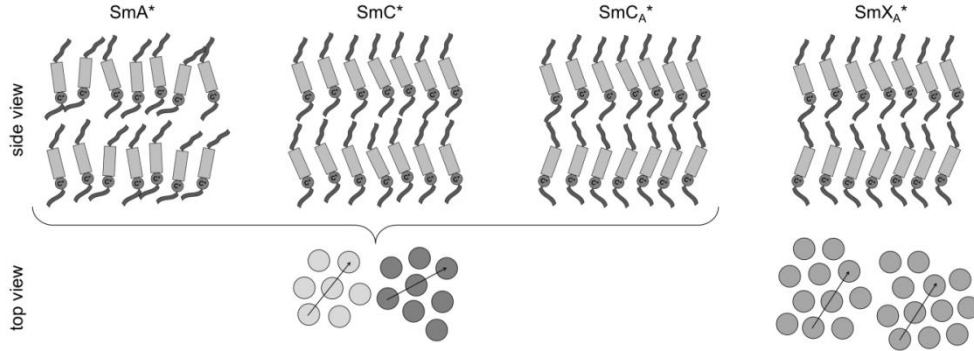


Figure 2. Schemes of the molecular arrangement in the selected smectic phases.

In the  $SmA^*$  phase, the average tilt  $\theta_o$  of molecules within the smectic layers is equal to zero, while in the  $SmC^*$ ,  $SmC_A^*$  and  $SmX_A^*$  phases,  $\theta_o > 0$  [7]. The subscript “O” refers to “optical” and indicates the tilt angle measured by the electro-optic (Clark-Lagerwall) method [8]. The optical tilt angle  $\theta_o$ , describing the tilt of the molecular cores, may be different than the steric tilt angle  $\theta_s$ , calculated from the molecular length and the smectic layer spacing [9-13]. The order of the tilt direction in the  $SmC^*$ , and  $SmC_A^*$  phases is approximately synclinal and anticlinical, respectively [14,15]. Small deviations from the ideal syn- or anticlinical order are caused by an additional helical change in the tilt direction, with the helical pitch at the order of 100-1000 nm [2,4]. The intra-layer positional order of molecules in the  $SmA^*$ ,  $SmC^*$  and  $SmC_A^*$  phases is the short-range one. The hexatic  $SmX_A^*$  phase also shows the bond-orientational order, which means that all domains with a local hexagonal ordering are oriented in the same direction within the smectic layer [7].

The tilt angle  $\theta_o$ , measured in the  $SmC_A^*$  phase for the  $mX_1X_2n$  compounds and their mixtures, is  $\sim 45^\circ$  [2,4,16]. It is a desired property for an antiferroelectric liquid crystal intended for application in displays because it prevents light leakage in the dark state of a display [17-19]. Another interesting property is that in some  $mX_1X_2n$  compounds, the glass transition (vitrification) of the  $SmC_A^*$  or hexatic  $SmX_A^*$  phase is detected, which is followed by the cold crystallization after reheating above the glass transition temperature [5,6,20-23]. Glassformers undergoing the cold crystallization may serve as materials for energy storage [24,25].

The subject of this paper is the 7HH6 compound, which forms the glass of the hexatic  $\text{SmX}_A^*$  phase. The phase sequence of 7HH6 during heating after vitrification of the smectic phase is  $\text{glSmX}_A^*$  (229 K)  $\text{SmX}_A^*$  (252 K) Cr2 (271 K) Cr1 (329 K)  $\text{SmC}_A^*$  (390 K)  $\text{SmC}^*$  (394 K)  $\text{SmA}^*$  (396 K) Iso, [23]. The purpose of the present study is the application of the X-ray diffraction (XRD) method to confirm the reported phase sequence and to determine the structural parameters of the smectic phases. The temperature dependence of the smectic layer spacing and the molecular models obtained by density-functional theory (DFT) calculations are applied to obtain the tilt angle of molecules and compare it with the values determined earlier by the electro-optic method [16]. The most probable molecular conformations are selected based on comparing the tilt angle determined by two different methods. Subsequently, these molecular models are used to calculate the vibrational modes and to interpret the experimental infra-red (IR) spectra. The IR spectroscopy results obtained for various temperatures serve to investigate the changes in the intra-molecular vibrations upon the glass transition, cold crystallization, melting and transition to the isotropic liquid phase of the 7HH6 compound.

## 2. Experimental and computational details

The synthetic route of (S)-4'-(1-methylheptylcarbonyl)biphenyl-4-yl 4-[5-(2,2,3,3,4,4,4-heptafluorobutoxy) heptyl-1-oxy]benzoate, abbreviated herein as 7HH6, is described in [1,2].

The X-ray diffraction measurements were carried out with the Empyrean 2 (PANalytical) diffractometer with the Cryostream 700 (Oxford Cryosystems) temperature attachment. The sample was heated to the isotropic liquid phase and placed in the glass capillary with a 0.3 mm diameter using the capillary effect. After inserting into the diffractometer, the sample was heated to 363 K, to the  $\text{SmC}_A^*$  phase, and cooled down to 183 K with the 6 K/min rate. The patterns were collected in the geometry of the horizontal rotating capillary, in the angular range  $2\theta = 2-30^\circ$ , upon heating from 183 K to 403 K. The programs used for data analysis were WinPLOTR [26] and OriginPro.

The FT-IR measurements were performed with the Bruker VERTEX 70v FT-IR spectrometer with Advanced Research System DE-202A cryostat and ARS-2HW compressor. The sample was mixed with KBr. The spectra were collected in the  $450-4000\text{ cm}^{-1}$  range with the  $2\text{ cm}^{-1}$  resolution and 32 scans per spectrum. The measurements were done in a vacuum upon the 1<sup>st</sup> heating of the pristine sample from 293 K to 408 K. Then the sample was cooled down directly to 173 K at 3 K/min and measurements were done on the 2<sup>nd</sup> heating to 408 K. The data analysis, including the peak fitting and k-means cluster analysis [27], was done in OriginPro.

The optimization of the molecular models and calculation of the vibrational modes were done using the Gaussian 16 program [28]. The selected basis set was def2TZVPP [29], and the exchange-correlation functional was B3LYP-D3(BJ) [30-33]. The Avogadro program [34] was used to prepare models and their visualization.

### 3. Results and discussion

#### 3.1. Structural changes investigated by X-ray diffraction

The XRD pattern of the 7HH6 sample cooled down to 183 K with the 6 K/min rate consists of a sharp peak at  $2\theta \approx 5.1^\circ$  and a wide diffuse maximum at  $2\theta \approx 20^\circ$  (Figure 3a). Subtraction of the isotropic liquid pattern at low angles also reveals another peak at  $2\theta \approx 2.6^\circ$ . Two low-angle diffraction peaks arise from the smectic layer order with the layer spacing  $d$  obtainable from the Bragg equation  $l\lambda = 2d \sin \theta$  [35], where  $l$  is the peak order (1<sup>st</sup> and 2<sup>nd</sup> for  $2\theta \approx 2.6^\circ$  and  $5.1^\circ$ ) and  $\lambda$  is the CuK $\alpha$  wavelength. The cold crystallization is observed at 253 K, although the fraction of the crystal phase is very small. At 263 K, a new low-angle diffraction peak at  $2\theta \approx 2.3^\circ$  arises, corresponding to the layer spacing in the crystal phase. The diffraction peaks from the crystal phase become sharper upon further heating, but no transition in the solid state is observed. Two crystal phases were observed in the differential scanning calorimetry experiments performed during constant heating at 2-20 K/min rates [23]. However, in the XRD experiment, the sample crystallizes directly into the high-temperature crystal phase. The 1<sup>st</sup>, 2<sup>nd</sup>, and 3<sup>rd</sup> order peaks from the layer spacing in the crystal phase were used to calculate the  $d$  value by fitting the formula:

$$\theta_l = \theta_0 + \arcsin\left(\frac{l\lambda}{d}\right) \quad (1)$$

to the plot of the peak positions vs. the peak order ( $l = 1, 2, 3$ ). The fitting includes the shift in the peak positions  $\theta_0$ , for correction of the systematic shift in  $d$ . The  $\theta_0 \approx -0.004^\circ$  value determined for the crystal phase was also applied to the smectic phases, where only one or two diffraction peaks related to the smectic layer spacing were visible. The XRD patterns of the SmC<sub>A</sub>\* phase are similar to those in the supercooled smectic phase. However, the diffuse maximum at higher angles is wider. Only the diffuse maximum is visible in the isotropic liquid, while no low-angle peaks are observed.

In the 183-263 K range, the smectic layer spacing has a maximum of 35.0(1) Å at 233 K (Figure 3b), which is close to the glass transition temperature  $T_g = 229$  K determined from the dielectric spectra of 7HH6 [23]. In the vitrified state,  $d$  increases on heating with a slope of 0.011(1) Å/K, while above  $T_g$  there is a decrease of  $d$  with a slope of  $-0.017(2)$  Å/K. The change in the temperature dependence of the characteristic distance at  $T_g$  was also reported, e.g., for cyclo-octanol [36]. Upon the cold crystallization, the layer spacing increases by almost 3 Å. In the crystal phase,  $d$  is independent of temperature, and its mean value is 37.56(2) Å. After melting, the layer spacing drops to 32.5 Å, smaller than 34.5 Å during the cold crystallization. The  $d$  value increases with increasing temperature until the transition to the SmA\* phase, where  $d$  is approximately constant, with the mean value 36.4(6) Å. The SmC<sub>A</sub>\*  $\rightarrow$  SmC\* transition is weakly visible as an increase in  $d$  between 388 K and 389 K, while at the SmC\*  $\rightarrow$  SmA\* transition between 394 K and 395 K, the smectic layer spacing increases by 5.4% (if  $d_{SmA^*}$  is considered as 100%). It is too much to classify the SmA\* phase of 7HH6 as the de Vries phase with a large tilt of molecules in random directions [37,38].

The ratio of the integrated intensities  $I_{002}$  and  $I_{001}$  of the 2<sup>nd</sup> and 1<sup>st</sup> order peaks related to the smectic layer order decreases with increasing temperature: the 1<sup>st</sup> order peak increases in intensity, while the 2<sup>nd</sup> order peak becomes smaller and disappears in the SmA\* phase. The  $I_{002}/I_{001}$  ratios shown in Figure 3c were corrected by the Lorentz-polarization factor [39] for each peak, as this factor strengthens the observed intensities at low angles. However, the uncorrected  $I_{002}/I_{001}$  ratios, although they are smaller than after correction, have qualitatively the same dependence on temperature. The  $I_{002}/I_{001}$  values decrease exponentially on heating. This is especially well-visible in the logarithmic scale, where the dependence becomes linear. The fitting parameters of the  $I_0 \exp(kT)$  function are  $I_0 = 90(10)$  and  $k = -0.0166(4)$  1/K. The  $I_{002}/I_{001}$  ratio seems insensitive to the glass transition and it also follows the same temperature dependence in the SmX<sub>A</sub>\* and SmC<sub>A</sub>\* phases in the investigated temperature range.

The diffuse maximum at  $2\theta \approx 20^\circ$  is more conveniently analyzed when plotted against the scattering vector  $q = 4\pi \sin \theta / \lambda$ , where it is described by the Lorentzian peak function, located at  $q_0$  and with the full-width at half-height  $2/\xi$ , where  $\xi$  is the correlation length of the short-range positional order [7,40]:

$$I(q) = \frac{A}{1 + \xi^2(q - q_0)^2} + Bq + C. \quad (2)$$

The  $A$  parameter is the height of the diffuse maximum,  $B$  and  $C$  are the parameters of the linear background, and the average distance between molecules can be determined as  $w = 2\pi/q_0$ . There are differences between the results for the supercooled state and those obtained above the melting temperature of a crystal  $T_m$  (Figure 3d). In the supercooled and vitrified smectic phase,  $w = 4.4\text{-}4.5$  Å and  $\xi = 11.2\text{-}11.9$  Å indicate significant nearest-neighbor and next-nearest-neighbor interactions within the smectic layers. Above the melting temperature of a crystal,  $w = 4.7\text{-}4.8$  Å and  $\xi = 4.3\text{-}5.0$  Å in the smectic phases and  $w = 4.9$  Å and  $\xi = 4.0$  Å in the isotropic liquid, which means only nearest-neighbor interactions. The intermolecular distance matches the molecular width, which is a commonly obtained result [5,41,42]. The matter of discussion is the identification of the smectic phase which undergoes the vitrification for 7HH6, i.e. whether it is the SmC<sub>A</sub>\* phase with only short-range positional order within layers, or the hexatic SmX<sub>A</sub>\* phase (SmF<sub>A</sub>\* or SmI<sub>A</sub>\* – indistinguishable based on the 1D XRD patterns), where the short-range order has a broader range and the bond-orientational order arises [7]. The differential scanning calorimetry results presented in [23] indicate the SmC<sub>A</sub>\*  $\rightarrow$  SmX<sub>A</sub>\* transition at 263.5 K during cooling. This is visible as a small endothermic anomaly with the enthalpy change of  $-0.34$  kJ/mol. The XRD results also show that the correlation length in the 183-263 K range is twice as large as for the SmC<sub>A</sub>\* phase above  $T_m$ . In similar compounds, which form the SmC<sub>A</sub>\* glass, the correlation length in the vitrified state reaches only 5.2-5.5 Å and does not differ much from the  $\xi$  values at higher temperatures [5]. Another indication of the SmX<sub>A</sub>\* phase is an increase of the layer spacing in the supercooled state compared to the SmC<sub>A</sub>\* above  $T_m$ . The increase of  $d$  was reported for other compounds where the transition to the hexatic

phase was directly visible in the XRD patterns [10,43-45]. On the other hand, in the XRD patterns of the hexatic phases, the maximum at  $2\theta \approx 20^\circ$  is expected to be sharper (with a spiky peak) [43,46] than the one obtained here for 7HH6. Also,  $\xi \approx 11-12 \text{ \AA}$  in the vitrified smectic phase of 7HH6 is a rather low value, since even for the simplest SmA phase, larger intra-layer correlations are reported for some compounds [46,47].

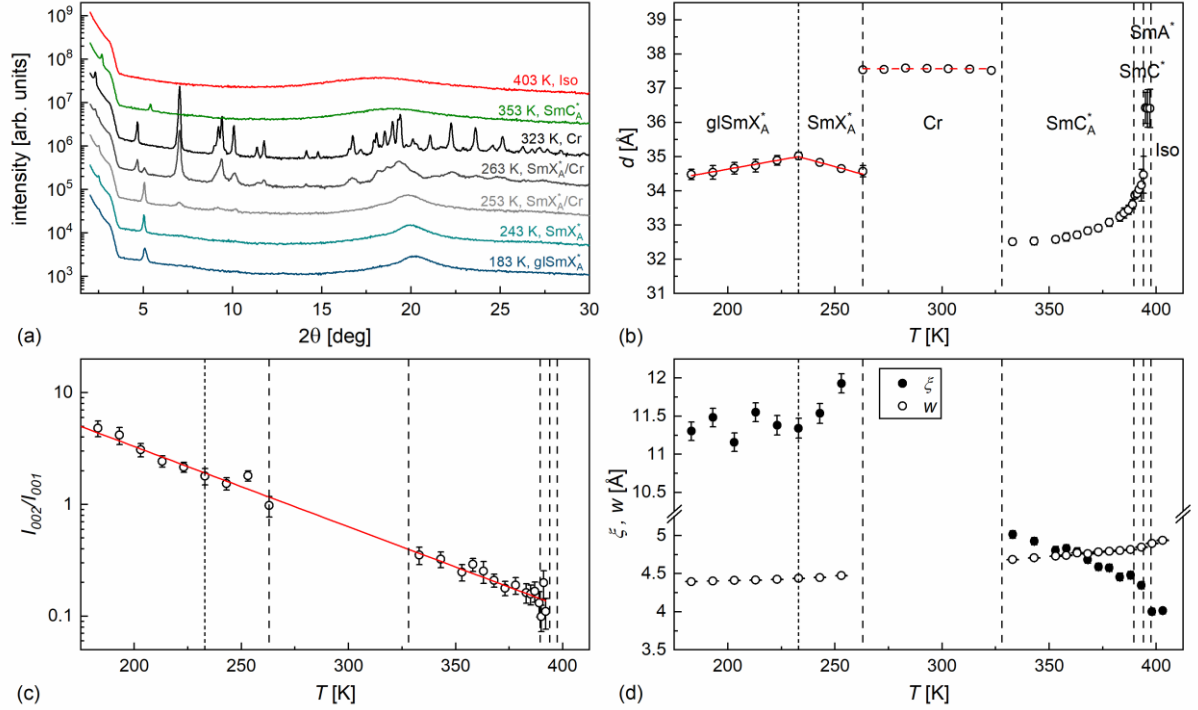


Figure 3. XRD patterns of 7HH6 collected on heating after direct cooling from the  $\text{SmC}_A^*$  phase to the vitrified smectic phase with the 6 K/min rate (a) and the temperature dependence of the layer spacing in the smectic and crystal phases (b), ratio of integrated intensities of the (002) and (001) peaks in the smectic phases, corrected by the Lorentz-polarization factor (c) and the correlation length and average intermolecular distance in the smectic and isotropic liquid phases (d).

### 3.2. Tilt angle and selection of molecular models

The 7HH6 compound forms the orthoconic  $\text{SmC}_A^*$  phase, where the tilt angle of molecules  $\theta_O$ , determined by the electro-optic method, reaches  $44^\circ$  [16]. The tilt angle decreases with increasing temperature, corresponding to the increasing layer spacing, and attempts are made to find a relationship between these parameters [9-13,48-51]. For the rod-like molecules, the optical tilt angle  $\theta_O$  is equal to the steric tilt angle  $\theta_S = \arccos(d/L)$ , where  $L$  is the molecular length obtained from molecular modeling or from the layer spacing in the SmA phase with a high orientational order parameter. However, the smectic phases are also formed by molecules with other shapes, like the hockey-stick, zig-zag or C-shape, which gives the molecular core a different orientation than the

whole molecule. In calculation of  $\theta_O$ , the tilt of the core is important [9-12]. This is why the applied formula is [48]:

$$\theta_O = \theta_S + \delta\theta = \arccos(d/L) + \delta\theta, \quad (3)$$

where  $\delta\theta$  is the shape parameter, equal to an angle between the direction of the whole molecule and direction of the aromatic core. Several molecular conformations were tested in [48] to check which one enables the best reproduction of  $\theta_O$  from the layer spacing obtained by XRD. In this paper, another approach is applied: the layer spacing from XRD is plotted against the tilt angle from electro-optic measurements (Figure 4a) and fitted with the formula:

$$d = L \cos(\theta_O - \delta\theta), \quad (4)$$

which enables determination of  $L$  and  $\delta\theta$ . The knowledge of these parameters is further used to infer the most likely conformations of the molecule. For 7HH6 the fitting results are  $L = 34.2(2)$  Å and  $\delta\theta = 25.1(8)^\circ$  in the SmC<sub>A</sub>\* phase, and  $L = 35.6(4)$  Å and  $\delta\theta = 19(2)^\circ$  in the SmC\* phase. The increase of the molecular length and decrease of the shape parameter at the SmC<sub>A</sub>\* → SmC\* transition indicate that molecules take a more extended shape in SmC\*. The  $L$  values are smaller than the layer spacing 36.4(6) Å in SmA\*, indicating that in the SmA\* phase, molecules have a more extended conformation. In both SmC<sub>A</sub>\* and SmC\* phases, the difference between the overall tilt of molecules and the tilt of the aromatic core is significant, as it equals more than half of  $\theta_O$ . The fitting with an assumption of the rod-like molecule with  $\delta\theta = 0$ , performed as a test, gives results in a considerable disagreement with the experimental data. In some papers, the discrepancy between  $\theta_O$  and  $\theta_S$  is explained by the dimer formation, where the length of a dimer exceeds the length of a single molecule [13,49,50]. However, for 7HH6 the fitting  $L$  values indicate that the main building block is a single molecule, not a dimer.

The main purpose is to find the molecular models with the  $L$  and  $\delta\theta$  values close to the fitting results of the (4) formula. The DFT results show at least two such models (Figure 3b). The definitions of  $L$  and  $\delta\theta$  and the molecular conformations included in this analysis are the same as in [48]. The length of a molecule  $L$  is equal to  $L_0 + L_{CF}$ , where  $L_0$  is the length of the  $\vec{L}_0$  vector from the terminal C atom in the chiral chain to this terminal F atom in the achiral chain which lies approximately in the same plane as the preceding C atoms, and  $L_{CF} = 3.22$  Å is the non-bonding distance between C and F [51]. The orientation of the aromatic core is described by the  $\vec{A}$  vector from the C atom in the COO group, located near the C\* atom, to the O atom adjacent to the benzene ring. The shape parameter  $\delta\theta$  is an angle formed by the  $\vec{L}_0$  and  $\vec{A}$  vectors (Figure 5a). The torsional angles selected for the optimization are the  $\varphi_1$  angle formed by the C(H<sub>2</sub>)-C(H<sub>2</sub>)-C\*(HCH<sub>3</sub>)-O atoms and describing the orientation of the chiral terminal chain, as well as the  $\varphi_2$  and  $\varphi_3$  angles formed by the C(H<sub>2</sub>)-O-C(H<sub>2</sub>)-C(F<sub>2</sub>) and O-C(H<sub>2</sub>)-C(F<sub>2</sub>)-C(F<sub>2</sub>) atoms, describing the orientation of the fluorinated part of the achiral terminal chain (Figure 5b).

Using the three local minima in the conformation energy for each torsional angle (Figure 5b), 27 final molecular models were obtained, and for each model, the tilt angle from the (3) formula was determined (Table 1). Eight models are giving at 333 K the  $\theta_O$  angle which agrees, within the  $\pm 2^\circ$  error, with  $\theta_O = 43.8^\circ$  measured electro-optically at the same temperature in Ref. [16]. Among them, only models 3 and 19 reproduce correctly the  $\theta_O(T)$  dependence in almost the whole considered temperature range, except the proximity of the  $\text{SmC}^*/\text{SmA}^*$  transition. The model 19 has a lower conformational energy, on the other hand, the model 3 was considered more probable in [48], as it led to correct  $\theta_O$  values for both compounds investigated therein. Different  $L$  and  $\delta\theta$  obtained for both phases in Figure 4a indicate that the molecular conformations in the  $\text{SmC}_A^*$  and  $\text{SmC}^*$  phase slightly differ. Interestingly,  $L_3 < L_{19}$  and  $\delta\theta_3 > \delta\theta_{19}$ , which agrees with the relationships between the  $L$  and  $\delta\theta$  values for the  $\text{SmC}_A^*$  and  $\text{SmC}^*$  phases. Models 3 and 19 correspond to the same local energy minimum for the  $\varphi_2$  angle. The changes in the  $\varphi_1$  and  $\varphi_3$  angles, necessary for transition between these models, are related to the energy barriers of 16 kJ/mol and 18 kJ/mol. Thus, it is not certain whether the  $\text{SmC}_A^*/\text{SmC}^*$  transition is related to the change between these two particular conformation, because the enthalpy change at this transition is negligible ( $>1$  kJ/mol [2,23]). The more likely explanation is that the  $\text{SmC}_A^*/\text{SmC}^*$  transition does not involve the conformational changes in all molecules but rather the changes in the fractions of molecules taking particular conformations.

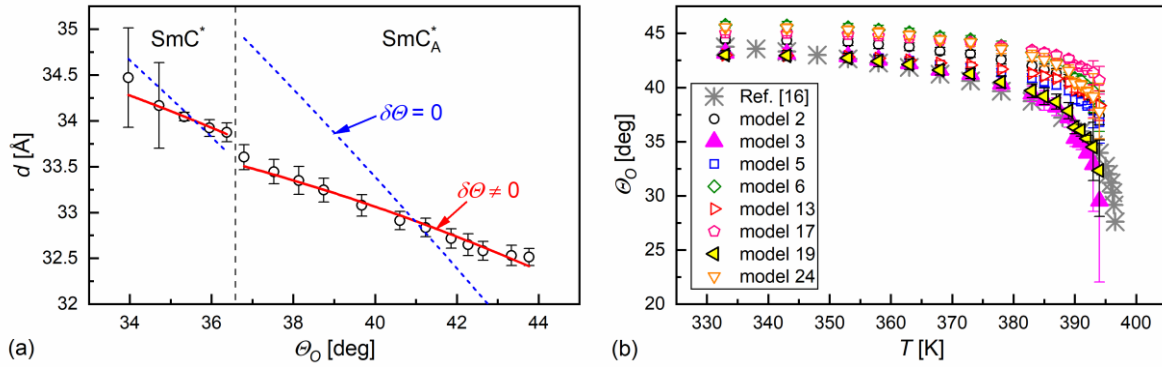


Figure 4. Smectic layer spacing determined from the XRD patterns (this work) vs. tilt angle measured by the electro-optic method at corresponding temperatures (values from Ref. [16]) with the fitting results of the (4) formula (a) and the tilt angle calculated from the (3) formula for various molecular models compared with the  $\theta_O$  values from Ref. [16] as a function of temperature (b).



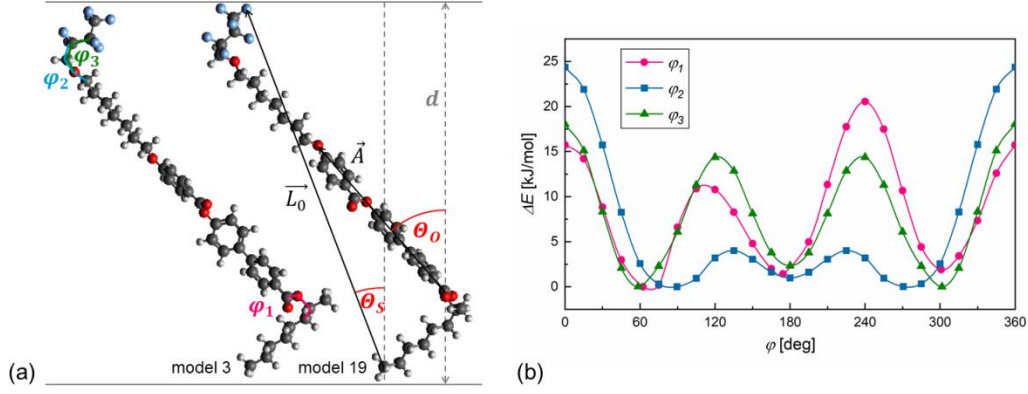


Figure 5. Molecular models 3 and 19 of 7HH6 with indicated torsional angles and vectors used in calculations of the tilt angle (a) and energy scans for torsional angles  $\varphi_1$ ,  $\varphi_2$ ,  $\varphi_3$  (b).

Table 1. DFT results (def2TZVPP basis set, B3LYP-D3(BJ) functional) for 27 conformations of the 7HH6 molecule, corresponding to local minima in energy presented in Figure 5b. For each conformation, the tilt angle was obtained according to the (3) formula, using the smectic layer spacing 32.5(1) Å in 333 K. The **bold** font indicates the models that agree, within the  $\pm 2^\circ$  error, with the experimental tilt angle of  $43.8^\circ$  [16] in 333 K.

model	$\Delta E$ [kJ/mol]	$\varphi_1$ [deg]	$\varphi_2$ [deg]	$\varphi_3$ [deg]	$L$ [Å]	$\delta\theta$ [deg]	$\theta_o$ [deg]
1	0.02	62.3	79.0	50.2	35.9	21.4	46.4(4)
2	<b>2.81</b>	<b>62.3</b>	<b>89.5</b>	<b>176.2</b>	<b>37.2</b>	<b>15.4</b>	<b>44.4(3)</b>
3	<b>4.17</b>	<b>62.3</b>	<b>109.9</b>	<b>294.7</b>	<b>34.7</b>	<b>22.6</b>	<b>43.2(5)</b>
4	1.48	62.4	181.3	58.5	36.6	12.9	35.1(4)
5	<b>3.79</b>	<b>62.4</b>	<b>180.0</b>	<b>180.1</b>	<b>38.0</b>	<b>11.8</b>	<b>43.1(3)</b>
6	<b>1.46</b>	<b>62.4</b>	<b>178.7</b>	<b>301.5</b>	<b>37.3</b>	<b>15.8</b>	<b>45.8(4)</b>
7	4.18	62.2	250.1	65.5	32.4	4.2	-
8	2.83	62.4	270.6	184.2	36.6	9.8	37.0(4)
9	0	62.2	281.0	309.9	33.8	4.9	20.6(6)
10	1.45	174.4	78.9	50.5	40.6	13.6	50.5(3)
11	4.24	174.3	90.2	176.8	42.5	10.1	50.3(2)
12	5.64	174.4	110.1	294.5	39.4	15.1	49.5(3)
13	<b>2.87</b>	<b>174.2</b>	<b>181.5</b>	<b>58.4</b>	<b>41.2</b>	<b>5.1</b>	<b>43.0(3)</b>
14	5.21	174.2	180.5	180.2	43.4	6.2	47.6(2)
15	2.90	174.2	178.6	301.6	41.8	11.2	50.0(2)
16	5.61	174.3	250.0	65.4	38.2	2.0	33.7(3)
17	<b>4.25</b>	<b>174.4</b>	<b>270.5</b>	<b>184.1</b>	<b>42.2</b>	<b>5.5</b>	<b>45.0(2)</b>
18	1.43	174.4	280.8	309.8	39.6	0.5	35.4(3)
19	<b>1.89</b>	<b>300.9</b>	<b>78.9</b>	<b>50.0</b>	<b>35.2</b>	<b>20.3</b>	<b>43.0(4)</b>
20	4.72	300.9	89.8	176.3	36.6	13.2	40.5(4)
21	6.08	300.8	109.6	294.5	33.9	21.0	37.2(6)
22	3.36	300.8	181.1	58.4	35.8	13.4	38.1(4)
23	5.70	300.9	180.3	180.1	37.5	10.9	40.8(3)
24	<b>3.37</b>	<b>300.7</b>	<b>178.9</b>	<b>301.5</b>	<b>36.6</b>	<b>18.4</b>	<b>45.6(4)</b>
25	6.10	300.8	250.5	65.5	32.1	5.6	-
26	4.73	300.9	269.5	183.1	35.9	6.9	32.2(4)
27	1.92	300.8	281.1	309.9	33.6	7.6	22.4(7)

### 3.3. Vibrational modes investigated by Fourier-transform infra-red spectroscopy

The theoretical IR spectra were calculated for the molecular models 3 and 19 selected in the previous section (Figure 6a). Each model enables the band assignment of the experimental IR spectra collected in the  $\text{SmC}_A^*$  phase at 333 K (Table 2). The bands in the  $513\text{-}661\text{ cm}^{-1}$  range correspond mainly to the scissoring and rocking vibrations in the terminal chains, as well as in-plane and out-of-plane deformations of the aromatic rings,  $692\text{-}771\text{ cm}^{-1}$  to the  $\text{CH}_2$  rocking and out-of-plane deformations of the aromatic rings,  $815\text{-}912\text{ cm}^{-1}$  to the rocking and stretching vibrations in the aromatic chains, and out-of-plane deformations of the aromatic rings,  $961\text{-}1070\text{ cm}^{-1}$  to the C-C, C-O stretching and in-plane deformations of the aromatic rings,  $1111\text{-}1275\text{ cm}^{-1}$  to the  $\text{CH}_2$  rocking and wagging, C-C, C-O, C-F stretching, and in-plane deformations of the aromatic rings,  $1314\text{-}1422\text{ cm}^{-1}$  to the  $\text{CH}_2$  twisting and wagging, and in-plane deformations of the aromatic rings, and  $1510\text{-}1607\text{ cm}^{-1}$  to the  $\text{CH}_2$  scissoring and in-plane deformations of the aromatic rings. The band at  $1711\text{ cm}^{-1}$  is attributed to the C=O stretching in the  $\text{COO}(\text{h})$  group next to the chiral center, and the band at  $1733\text{ cm}^{-1}$  to the C=O stretching in the  $\text{COO}(\text{e})$  spacer within the aromatic core. The bands in  $2862\text{-}2981\text{ cm}^{-1}$  and  $3042\text{-}3074\text{ cm}^{-1}$  correspond to the C-H stretching in the terminal chains and in the aromatic rings, respectively. The overall scaling factor between the calculated and experimental wavenumbers, obtained based on the DFT results for both models (Figure 6b), equals  $0.969(2)$ . Since the scaling may vary between different frequency ranges [52], the scaling factor was also obtained separately for experimental values  $>1000\text{ cm}^{-1}$ ,  $1000\text{-}2000\text{ cm}^{-1}$  and  $>2000\text{ cm}^{-1}$ , and is equal to  $0.977(3)$ ,  $0.986(2)$  and  $0.955(2)$ , respectively. Thus, the most significant overestimation in the calculated wavenumbers occurs for the bands originating from the C-H stretching. The corresponding results for the IR spectrum of the pristine sample at 293 K are presented in Electronic Supplementary Materials together with atomic coordinates and IR spectra calculated for the models 3 and 19. The scaling factors for the pristine sample at 293 K agree within uncertainties with these for the  $\text{SmC}_A^*$  phase at 333 K.

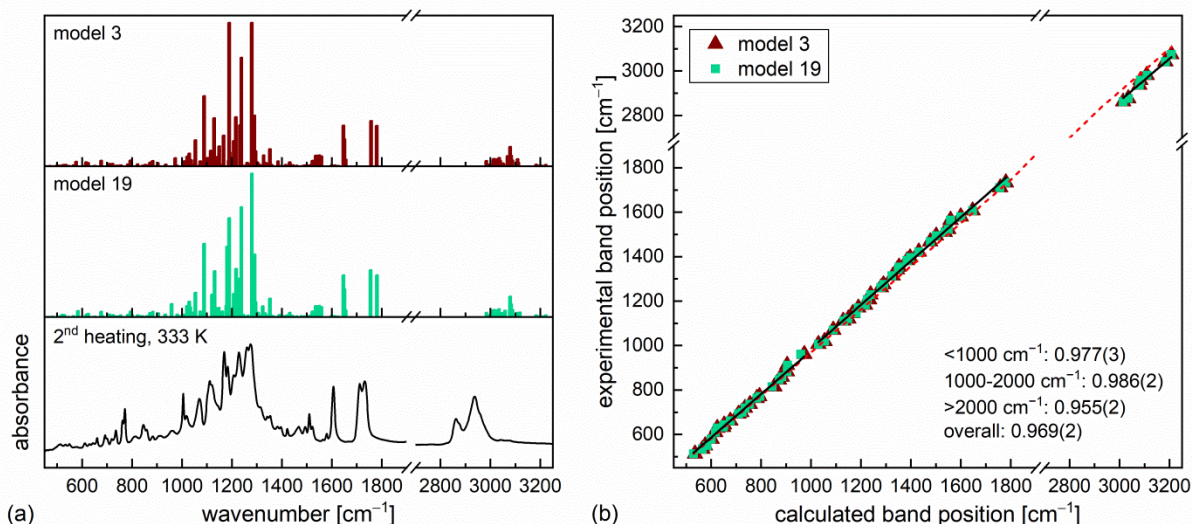


Figure 6. The IR spectrum of 7HH6 collected upon the 2<sup>nd</sup> heating at 333 K compared to the unscaled calculated spectra for the molecular models 3 and 19 (DFT, def2TZVPP basis set, B3LYP-D3(BJ) functional) (a) and scaling between the experimental and calculated band positions,  $\tilde{\nu}_{exp} = a\tilde{\nu}_{calc}$ , where  $a$  is the scaling factor (b).

Table 2. The band assignment of the experimental IR spectra of 7HH6 measured upon the 2<sup>nd</sup> heating at 333 K, based on the DFT calculations (def2TZVPP basis set, B3LYP-D3(BJ) functional). Experimental and calculated wavenumbers are given in  $\text{cm}^{-1}$ . The intra-molecular vibrations are denoted as follows:  $\beta$  – in-plane deformation,  $\gamma$  – out-of-plane deformation,  $\delta$  – scissoring,  $\nu$  – stretching,  $\rho$  – rocking,  $\tau$  – twisting,  $\omega$  – wagging.

experimental	model 3	model 19	interpretation
513	535.8	529.5	$\delta\text{CF}_2(\text{a}), \delta\text{COC}(\text{b,c}), \delta\text{CCC}(\text{c}), \gamma\text{Ph}(\text{f,g}), \delta\text{OCC}(\text{b,c})^{\text{model13}}, \beta_{\text{asym}}\text{Ph}(\text{d})^{\text{model13}}, \gamma\text{Ph}(\text{d})^{\text{model19}}$
534	565.4	565.1	$\gamma\text{Ph}(\text{f,g})$
550	576.2	584.0	$\delta\text{CF}_2(\text{a}), \delta\text{CCO}(\text{a,b})$
579	602.4	600.5	$\rho\text{CF}_2(\text{a}), \rho\text{CH}_2(\text{b})$
610	616.6	617.3	$\delta\text{CF}_2(\text{a}), \rho\text{CH}_2(\text{b})$
629	624.7	624.7	$\beta_{\text{asym}}\text{Ph}(\text{d,f,g})$
633	648.7	648.8	$\beta_{\text{asym}}\text{Ph}(\text{d,g}), \gamma\text{Ph}(\text{f})$
644	651.9	651.9	$\beta_{\text{asym}}\text{Ph}(\text{d,f,g})$
661	677.3	677.1	$\beta_{\text{asym}}\text{Ph}(\text{d,g}), \gamma\text{Ph}(\text{f})$
692	709.9	710.0	$\gamma\text{Ph}(\text{d})$
700	721.7	724.4	$\gamma\text{Ph}(\text{f,g})$
719	735.6	735.9	$\rho\text{CH}_2(\text{j})$
736	755.7	754.4	$\rho\text{CH}_2(\text{c})$
763	783.5	783.4	$\gamma\text{Ph}(\text{d})$
771	793.8	795.2	$\gamma\text{Ph}(\text{d,f,g}), \rho\text{CH}_2(\text{j})$
815	853.6	844.2	$\tau\text{CH}_2(\text{j})^{\text{model13}}, \gamma\text{Ph}(\text{f})^{\text{model19}}$
846	872.6	872.7	$\gamma\text{Ph}(\text{d})$
859	883.1	883.6	$\gamma\text{Ph}(\text{f,g})$
883	904.1	904.5	$\nu\text{CC}(\text{a,b})^{\text{model13}}, \rho\text{CH}_2(\text{b})^{\text{model13}}, \gamma\text{Ph}(\text{f,g})^{\text{model19}}$
912	904.2	906.0	$\gamma\text{Ph}(\text{f,g})^{\text{model13}}, \nu\text{CC}(\text{a,b})^{\text{model19}}, \rho\text{CH}_2(\text{b})^{\text{model19}}$

961	973.7	959.1	$\nu_{\text{sym}}\text{COC}(\text{b,c}), \nu_{\text{sym}}\text{CCC}(\text{c})$
1006	1029.8	1029.7	$\beta_{\text{asym}}\text{Ph}(\text{d})$
1019	1054.4	1054.6	$\nu_{\text{asym}}\text{CCC}(\text{c}), \nu\text{CO}(\text{c}), \beta_{\text{asym}}\text{Ph}(\text{d,f,g})$
1070	1089.4	1089.3	$\beta_{\text{asym}}\text{Ph}(\text{d,f}), \nu\text{CO}(\text{e})$
1111	1129.3	1131.6	$\beta_{\text{asym}}\text{Ph}(\text{g}), \nu_{\text{asym}}\text{COC}(\text{h,i})$
1121	1149.8	1147.9	$\nu_{\text{asym}}\text{CF}_2(\text{a}), \nu_{\text{sym}}\text{CCC}(\text{c}), \beta_{\text{sym}}\text{Ph}(\text{d}),$ $\nu_{\text{asym}}\text{COC}(\text{b,c})^{\text{model13}}, \rho\text{CH}_2(\text{b})^{\text{model19}}$
1145	1167.1	1181.5	$\nu_{\text{asym}}\text{CF}_2(\text{a}), \rho\text{CH}_2(\text{b}), \nu_{\text{asym}}\text{COC}(\text{b,c})^{\text{model19}}$
1170	1189.5	1189.5	$\beta_{\text{sym}}\text{Ph}(\text{d,f})$
1183	1216.6	1217.8	$\omega\text{CF}_2(\text{a}), \omega\text{CH}_2(\text{b})$
1207	1233.1	1225.7	$\nu_{\text{sym}}\text{CF}_2(\text{a}), \nu\text{CC}(\text{a}), \delta\text{CCC}(\text{a})$
1229	1238.5	1238.5	$\beta_{\text{sym}}\text{Ph}(\text{d,g}), \beta_{\text{asym}}\text{Ph}(\text{f}), \nu_{\text{asym}}\text{COC}(\text{e,f})$
1261	1280.4	1280.5	$\beta_{\text{asym}}\text{Ph}(\text{d,f}), \nu_{\text{asym}}\text{CCO}(\text{d,e})$
1275	1290.7	1291.7	$\beta_{\text{asym}}\text{Ph}(\text{g}), \nu_{\text{asym}}\text{CCO}(\text{g,h}), \delta\text{OC}^*\text{H}(\text{h,i})$
1314	1327.7	1323.9	$\omega\text{CF}_2(\text{a}), \tau\text{CH}_2(\text{b,c})$
1342	1345.2	1349.3	$\nu_{\text{sym}}\text{CCC}(\text{a}), \tau\text{CH}_2(\text{b,c}), \omega\text{CH}_2(\text{c}), \beta_{\text{asym}}\text{Ph}(\text{d})$
1354	1352.6	1353.0	$\tau\text{CH}_2(\text{b}), \omega\text{CH}_2(\text{c}), \beta_{\text{asym}}\text{Ph}(\text{d}), \tau\text{CH}_2(\text{c})^{\text{model19}}$
1383	1385.1	1385.1	$\omega\text{CH}_2(\text{i,j})$
1396	1397.3	1397.5	$\omega\text{CH}_2(\text{b,c})$
1422	1432.0	1432.3	$\omega\text{CH}_2(\text{c}), \beta_{\text{asym}}\text{Ph}(\text{d})$
1468	1477.9	1478.2	$\delta\text{CH}_2(\text{i,j})^{\text{model13}}, \delta\text{CH}_2(\text{b,c})^{\text{model19}}, \omega\text{CH}_2(\text{c})^{\text{model19}}$
1494	1501.1	1501.1	$\delta\text{CH}_3(\text{j})$
1510	1536.4	1536.5	$\beta_{\text{asym}}\text{Ph}(\text{f,g})$
1523	1550.0	1550.1	$\beta_{\text{asym}}\text{Ph}(\text{d})$
1565	1559.3	1559.3	$\beta_{\text{asym}}\text{Ph}(\text{f,g})$
1580	1600.3	1600.3	$\beta_{\text{asym}}\text{Ph}(\text{f,g})$
1607	1647.5	1647.5	$\beta_{\text{sym}}\text{Ph}(\text{d,f,g})$
1711	1758.2	1756.1	$\nu\text{C}=\text{O}(\text{h})$
1733	1780.8	1781.2	$\nu\text{C}=\text{O}(\text{e})$
2862	3014.7	3014.4	$\nu_{\text{sym}}\text{CH}_2(\text{c}), \nu_{\text{asym}}\text{CH}_2(\text{j})$
2876	3035.5	3034.9	$\nu_{\text{sym}}\text{CH}_2(\text{c}), \nu_{\text{sym}}\text{CH}_2(\text{b})^{\text{model13}}, \nu_{\text{asym}}\text{CH}_2(\text{c})^{\text{model19}}$
2937	3079.5	3079.4	$\nu_{\text{asym}}\text{CH}_2(\text{c})$
2959	3083.7	3083.3	$\nu_{\text{asym}}\text{CH}_2(\text{j})$
2981	3109.1	3110.0	$\nu\text{CH}_3(\text{i})$
3042	3183.6	3183.6	$\nu_{\text{asym}}\text{CH}(\text{f,g})$
3074	3208.1	3207.6	$\nu_{\text{sym}}\text{CH}(\text{f,g})$

Next, the temperature dependence of the experimental IR spectra is investigated. At the room temperature, the pristine 7HH6 sample is in the crystal phase. After the 1<sup>st</sup> heating to the isotropic liquid and cooling down with the 3 K/min rate to 173 K, the vitrified SmX<sub>A</sub>\* phase is obtained. Upon the 2<sup>nd</sup> heating, the cold crystallization and subsequent melting of the crystal phase are observed (Figure 7a). The bands from the C=O stretching are often sensitive to the phase transitions [21,53,54]. They are also well separated from other absorption bands, therefore, they could have been deconvolved by fitting the peak functions (Figure 7b-d). They are denoted as I, II, III, and IV in an order of an increasing wavenumber. There are four  $\nu\text{C}=\text{O}$  bands in the crystal phase, three in the SmX<sub>A</sub>\* phase and the SmX<sub>A</sub>\* glass, and two in the SmC<sub>A</sub>\* and Iso phases. The SmC\* and SmA\* phases have a narrow temperature range [23] and the IR spectrum collected at 393 K, which belongs to SmC\* or SmA\*, also shows two  $\nu\text{C}=\text{O}$  bands. Bands I and IV are observed in all phases, band III appears in the crystal and SmX<sub>A</sub>\* phases, while band II is observed only in the crystal phase (Figure

8). The appearance of additional  $\nu\text{C}=\text{O}$  bands is usually caused by inter- or intramolecular interactions, which have various effects: the hydrogen bonding shifts the  $\nu\text{C}=\text{O}$  band towards lower wavenumbers (redshift) [55-57]. In comparison, the proximity of the F atom shifts the  $\nu\text{C}=\text{O}$  band towards higher wavenumbers (blueshift) [58]. As 7HH6 is not fluorosubstituted in the molecular core, the latter effect can be caused only by proximity to a neighbor molecule's partially fluorinated terminal chain. The interpretation of bands I-IV is presented in Table 3. The bands I and IV are attributed to the  $\text{C}=\text{O}$  stretching in the COO groups (h) and (e), respectively, which are not close to the F atom. Both bands I and IV shift to higher wavenumbers upon heating above the melting temperature, which may be the effect of the breaking of very weak intermolecular hydrogen bonds involving the COO groups, e.g., of the  $\text{C}-\text{H}\dots\text{O}$  type. A lower wavenumber of band I below the melting temperature indicates stronger hydrogen bonding involving the COO (h) group in the  $\text{SmX}_A^*$  and Cr phases than in  $\text{SmC}_A^*$ . The decrease of the area and increase of band IV's peak position and the appearance of band III in the  $\text{SmX}_A^*$  phase suggest that a small fraction of molecules is not hydrogen-bonded. In contrast, most molecules form hydrogen bonds (stronger than in the  $\text{SmC}_A^*$  phase) involving the COO (e) group. The possible scenario is that the hydrogen bonds exist between the molecules forming clusters with a local hexagonal ordering, making them larger and more stable than in the  $\text{SmC}_A^*$  phase, and the molecules at the borders between clusters are not hydrogen-bonded. In the crystal phase, four  $\nu\text{C}=\text{O}$  bands indicate that the antisymmetric unit of the crystal structure probably contains two molecules with different surrounding, which are consequently involved in different intermolecular interactions. Thus, the presence of band II can be caused by the proximity between the COO (h) group from one molecule and the F atom from a neighbor molecule or by the lack of hydrogen bonding, and band III corresponds to the hydrogen-bonded COO (e) group.

Table 3. Interpretation of the experimental  $\text{C}=\text{O}$  stretching bands registered for 7HH6.

phase	I	II	III	IV
$\text{glSmX}_A^*/\text{SmX}_A^*$	COO(h) H-bonded	-	COO(e) weakly H-bonded	COO(e) not H-bonded
Cr	COO(h) H-bonded	COO(h) not H-bonded or close to F	COO(e) H-bonded	COO(e) not H-bonded
$\text{SmC}_A^*/\text{SmC}^*/\text{SmA}^*$	COO(h) weakly H-bonded	-	-	COO(e) weakly H-bonded
Iso	COO(h) not H-bonded	-	-	COO(e) not H-bonded

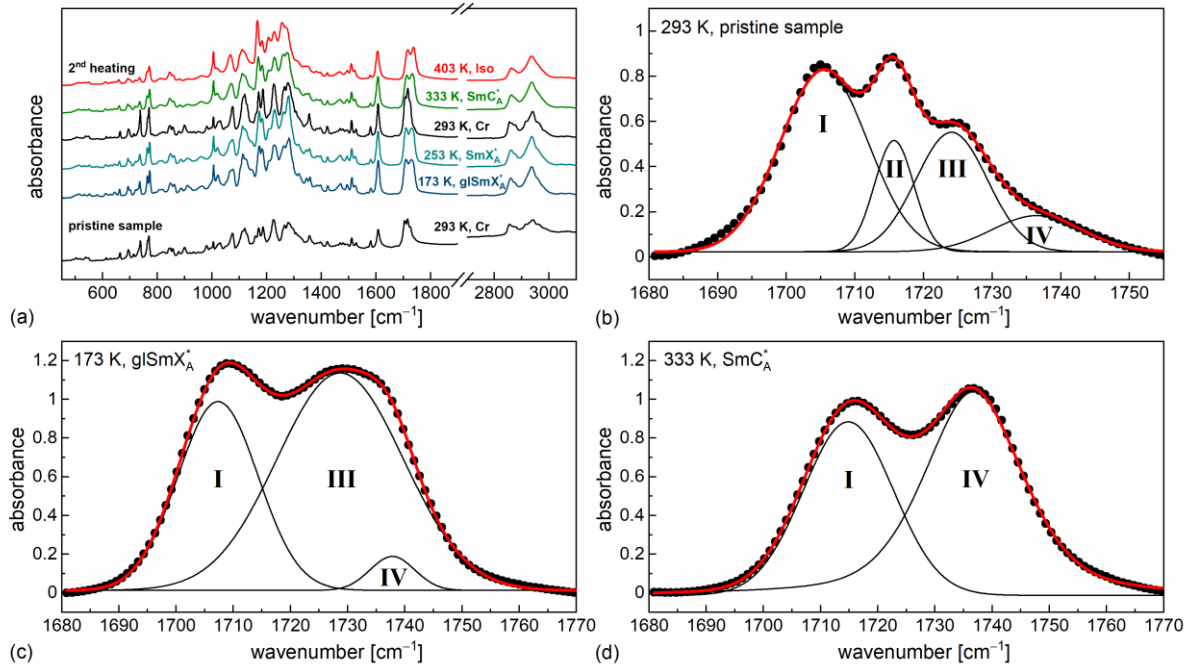


Figure 7. IR spectra of 7HH6 collected at 293 K for a pristine sample and upon heating from the vitrified  $\text{SmX}_A^*$  phase (a), and exemplary fits of pseudo-Voigt peak functions to the absorption bands related to the C=O stretching for the crystal phase at 293 K (a), vitrified  $\text{SmX}_A^*$  phase at 173 K (c) and  $\text{SmC}_A^*$  phase at 333 K (d). The results in (b) and (c,d) were obtained for the 1<sup>st</sup> and 2<sup>nd</sup> heating runs. The baseline was manually subtracted from (b-d) before fitting.

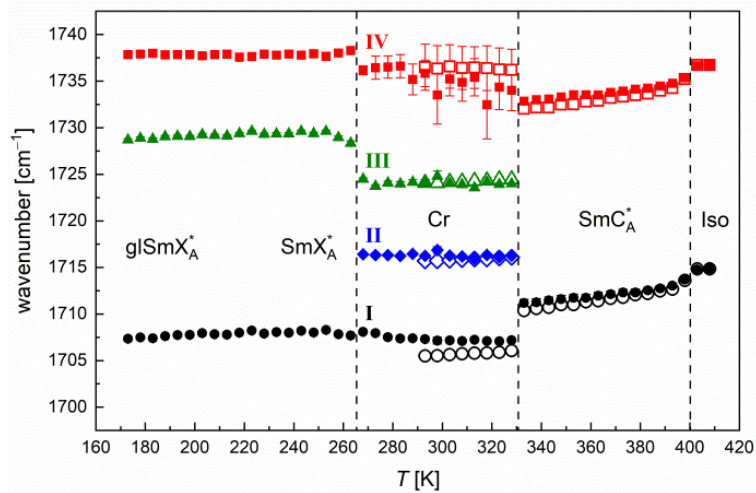


Figure 8. Wavenumbers of the  $\nu\text{C}=\text{O}$  bands vs. temperature, obtained from the IR spectra of 7HH6 collected upon the 1<sup>st</sup> heating of the pristine sample (open symbols) and 2<sup>nd</sup> heating of the vitrified sample (solid symbols). The  $\text{SmC}^*$  and  $\text{SmA}^*$  phases are not indicated in a narrow temperature range between  $\text{SmC}_A^*$  and Iso.

The positions of the  $\nu\text{C}=\text{O}$  bands are sensitive to the cold crystallization, melting and transition to the isotropic liquid of 7HH6, while they do not show a clear change at  $T_g$ . Also other parameters of the  $\nu\text{C}=\text{O}$  bands: area, half-width and height, when plotted as a function of temperature, are too scattered to reveal the glass transition. The exceptions are the height and area of the weak peak IV, which both show a minimum in the glass transition temperature region (Figure S2).

Better insight into the influence of phase transitions on the intra-molecular vibrations can be obtained by the k-means cluster analysis [27,59-62]. This method enables the segregation of data – in this case, the IR spectra collected at different temperatures – into mentioned clusters. The data within each cluster are maximally similar and differ maximally between the clusters [27,59-61]. The analysis can be done for the spectra in the whole  $450\text{-}4000\text{ cm}^{-1}$  range. However, as presented in the papers [61,62], performing it separately for selected spectral ranges is more informative. For the IR spectra registered as a function of temperature, one can infer which intra-molecular vibrations are more affected by the phase transition [61]. Thus, each IR spectrum of 7HH6 was divided into 10 parts (Figure 9) and a cluster analysis was performed on each one independently. The number of clusters optimal for a given dataset can be calculated using elbow method [59,60], based on the summed square error plotted vs. the number of clusters. The optimal number of clusters is presumed to be at the inflection point. The analysis by the elbow method for the IR spectra of 7HH6 in the  $1650\text{-}1850\text{ cm}^{-1}$  range suggests that the optimal number of clusters is 3 (Figure S3), and it was applied to the results in all spectral ranges (Figure 9a). Cluster 1 contains the IR spectra collected in the  $173\text{-}263\text{ K}$  or  $173\text{-}268\text{ K}$  temperature ranges ( $\text{SmX}_A^*$  and its glass), cluster 2 – spectra from  $268\text{-}328\text{ K}$  or  $273\text{-}328\text{ K}$  (crystal phase), and cluster 3 – spectra from  $333\text{-}408\text{ K}$  ( $\text{SmC}_A^*$ -isotropic liquid phases). The temperature of cold crystallization determined by the cluster analysis is  $\sim 268\text{ K}$ , which is higher than  $253\text{ K}$  observed in the XRD patterns. It is caused by the fact that the XRD measurement is slower than the IR spectroscopy one, therefore, the sample has time to crystallize at a lower temperature. The melting temperature of a crystal is in agreement with the XRD results.

In the next step, the IR spectra from  $268\text{-}328\text{ K}$  were excluded, and the cluster analysis was performed separately for the  $173\text{-}263\text{ K}$  and  $333\text{-}408\text{ K}$  ranges. For each temperature range, two clusters were assumed, corresponding to  $\text{glSmX}_A^*$ ,  $\text{SmX}_A^*$  for  $173\text{-}263\text{ K}$  and  $\text{SmC}_A^*$ , Iso for  $333\text{-}408\text{ K}$ . The 2-cluster analysis for  $173\text{-}263\text{ K}$  (Figure 9b) shows that the absorption bands from the  $1090\text{-}1300\text{ cm}^{-1}$  and  $1650\text{-}3200\text{ cm}^{-1}$  ranges are divided into two clusters in a random manner. This indicates that the experimental data's noise is stronger than any changes originating from the glass transition. The bands from the  $450\text{-}675\text{ cm}^{-1}$  and  $1300\text{-}1550\text{ cm}^{-1}$  ranges indicate  $T_g \sim 218\text{ K}$ , while bands from the  $675\text{-}1090\text{ cm}^{-1}$  and  $1550\text{-}1650\text{ cm}^{-1}$  ranges indicate  $T_g \sim 228\text{ K}$ . The latter is closer to  $T_g = 229\text{ K}$  determined from the dielectric spectra [23] and  $T_g = 233\text{ K}$  obtained in this work from the XRD patterns.

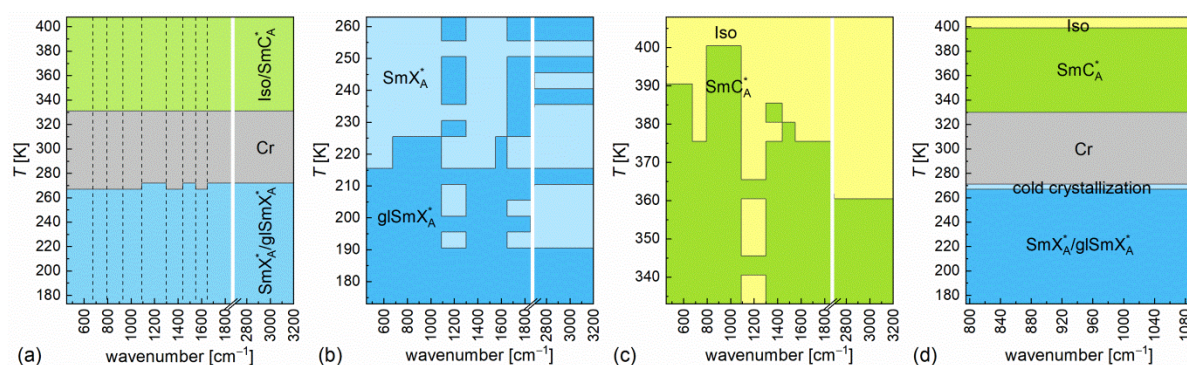


Figure 9. The phase sequence of the vitrified 7HH6 sample on heating determined by the k-means cluster analysis for various ranges in the IR spectra: 3-cluster analysis in the 173-403 K range (a), 2-cluster analysis in 173-263 K (b) and 333-408 K (c), and 5-cluster analysis in 173-403 K for the spectral range  $795\text{-}1090\text{ cm}^{-1}$ . The vertical dashed lines in the panel (a) indicate the separate spectral ranges.

The 2-cluster analysis for 333-408 K (Figure 9c) gives surprising results because only the absorption bands from the  $795\text{-}1090\text{ cm}^{-1}$  range are correctly divided into the  $\text{SmC}_A^*$  and Iso phases. Even for the  $\nu\text{C}=\text{O}$  bands, the border between clusters is at 378 K, much lower than the transition temperature to the isotropic liquid  $\sim 400\text{ K}$  determined from the  $\nu\text{C}=\text{O}$  band positions (Figure 8). It shows that a cluster analysis should not be used as the only way of data analysis because it can be inappropriate in some cases. For the  $\nu\text{C}=\text{O}$  bands, the indicator of the smectic – liquid transition is the change in the temperature dependence: increasing band position in  $\text{SmC}_A^*$  and constant in Iso, not the distances between values for which the algorithm is sensitive.

The bands in the  $795\text{-}1090\text{ cm}^{-1}$  range proved to be the most effective when used in the cluster analysis, as they gave satisfactory results both for 173-263 K and 333-408 K. They originate from the vibrations in the achiral chain (C-C, C-O stretching,  $\text{CH}_2$  rocking) and the aromatic core (in-plane and out-of-plane deformations). Only one band in this range may originate from the  $\text{CH}_2$  twisting in the chiral chain, according to molecular model 3 (Table 2). In the last step, the 5-cluster analysis was performed for the  $795\text{-}1090\text{ cm}^{-1}$  range for all temperatures, to check if the phase sequence can be reproduced (Figure 9d). However, while the IR spectra are correctly attributed to the Cr,  $\text{SmC}_A^*$  and Iso phases, the  $\text{SmX}_A^*$  and its glass are within the same cluster. The fifth cluster contains only the IR spectrum from 268 K, which corresponds to the cold crystallization and was attributed by the 3-cluster analysis either to the  $\text{SmX}_A^*$  or Cr phase (Figure 9a). It shows that in the investigation of the glass transition, it is more convenient to consider only the temperature range of the supercooled state because stronger effects related to the cold crystallization may disturb the cluster analysis.



## 4. Conclusions

The 7HH6 compound, forming four smectic phases: SmA\*, SmC\*, SmC<sub>A</sub>\*, and hexatic SmX<sub>A</sub>\*, was investigated by X-ray diffraction and IR spectroscopy:

- The transitions between the smectic phases and the glass transition of the SmX<sub>A</sub>\* phase are detectable in the temperature dependence of the smectic layer spacing. The ratio of the intensity of the 2<sup>nd</sup> and 1<sup>st</sup> order peaks, describing the smectic layer order, decreases logarithmically on heating, also below the glass transition temperature.
- The correlation length of the positional short-range order is unusually low in the SmX<sub>A</sub>\* phase, as it extends only to the next-nearest neighbors. However, it is larger than in the SmC<sub>A</sub>\* phase, where it corresponds only to the distance between the nearest-neighbors.
- By analysis of the smectic layer spacing in the SmC<sub>A</sub>\* and SmC\* phases as a function of the tilt angle, it is proven that the building block of the smectic layer is a single molecule (not a dimer) with the aromatic core tilted by ca. 20-25° in respect to the whole molecule. Thus, half of the high tilt angle exhibited by 7HH6 in the SmC<sub>A</sub>\* phase originates from the molecular shape.
- The molecular arrangement in the SmX<sub>A</sub>\* phase differs, as the smectic layer spacing is larger than in SmC<sub>A</sub>\*. Another sign of the structural changes affecting the intra-molecular interactions in SmX<sub>A</sub>\* is appearance of the third C=O stretching band, absent in SmC<sub>A</sub>\*, where two C=O stretching bands are observed, each originating from another COO group.
- The experimental positions of the C=O stretching bands, obtained as a function of temperature, suggest that the COO groups in some phases are involved in weak hydrogen bonds.
- The k-means cluster analysis enables the determination of the glass transition temperature only for some spectral ranges. The 795-1090 cm<sup>-1</sup> range, containing mainly the absorption bands originating from the vibrations in the achiral chain and aromatic core, is the most efficient for detecting the phase transitions by a cluster analysis.

It is planned to prepare the mixture of 3F7HPhH6 with MHPOBC, which also shows the hexatic smectic phase [63]. It will enable checking whether these compounds exhibit the same type of the SmX<sub>A</sub>\* phase (SmF<sub>A</sub>\* or SmI<sub>A</sub>\*).

### Authors' contributions:

A. Deptuch – conceptualization, investigation (XRD, DFT), formal analysis (XRD, FT-IR), writing – original draft.

N. Górska – investigation (FT-IR), writing – review and editing.

S. Baran – investigation (XRD), writing – review and editing.

M. Urbańska – resources (sample's synthesis), writing – review and editing.

**Declaration statement:** The authors declare no conflict of interest.

**Acknowledgements.** We thank Assoc. Prof. Ewa Juszyńska-Gałązka from Institute of Nuclear Physics Polish Academy of Sciences for the discussion regarding the data analysis and presentation, and Assoc. Prof. Wojciech Zajęc from Institute of Nuclear Physics Polish Academy of Sciences for help with the DFT calculations. We gratefully acknowledge Poland's high-performance Infrastructure PLGrid Academic Computer Centre Cyfronet AGH for providing computer facilities and support within the computational grant. Empyrean 2 (PANalytical) diffractometer with Cryostream 700 Plus (Oxford Cryosystems) temperature attachment were purchased thanks to European Regional Development Fund Operational Program Infrastructure and Environment (contract no. POIS.13.01.00-00-062/08). Bruker VERTEX 70v FT-IR spectrometer with Advanced Research System DE-202A cryostat and ARS-2HW compressor were purchased thanks to the European Regional Development Fund in the framework of the Innovative Economy Operational Program (contract no. POIG.02.01.00-12-023/08). This research was supported in part by the Excellence Initiative – Research University Program at the Jagiellonian University in Kraków.

### Bibliography

- [1] M. Żurowska, R. Dąbrowski, J. Dziaduszek, K. Czupryński, K. Skrzypek, M. Filipowicz, Synthesis and Mesomorphic Properties of Chiral Esters Comprising Partially Fluorinated Alkoxyalkoxy Terminal Chains and a 1-methylheptyl Chiral Moiety, *Mol. Cryst. Liq. Cryst.* 495 (2008) 145/[497]-157/[509], <https://doi.org/10.1080/15421400802432428>.
- [2] M. Żurowska, R. Dąbrowski, J. Dziaduszek, K. Garbat, M. Filipowicz, M. Tykarska, W. Rejmer, K. Czupryński, A. Spadło, N. Bennis, J.M. Otón, Influence of alkoxy chain length and fluorosubstitution on mesogenic and spectral properties of high tilted antiferroelectric esters, *J. Mater. Chem.* 21 (2011) 2144-2153, <https://doi.org/10.1039/C0JM02015J>.
- [3] K. Milewska, W. Drzewiński, M. Czerwiński, R. Dąbrowski, Design, synthesis and mesomorphic properties of chiral benzoates and fluorobenzoates with direct  $\text{SmC}_A^*$ -Iso phase transition, *Liq. Cryst.* 42 (2015) 1601-1611, <https://doi.org/10.1080/02678292.2015.1078916>.
- [4] M. Tykarska, M. Czerwiński, A. Drzewicz, Effect of molecular structure and temperature on the helical pitch and handedness in antiferroelectric liquid crystalline phase, *J. Mol. Liq.* 292 (2019) 110379, <https://doi.org/10.1016/j.molliq.2019.01.148>.
- [5] A. Deptuch, M. Marzec, T. Jaworska-Gołąb, M. Dziurka, J. Hooper, M. Srebro-Hooper, P. Fryń, J. Fitas, M. Urbańska, M. Tykarska, Influence of carbon chain length on physical properties of 3FmHPHF homologues, *Liq. Cryst.* 46 (2019) 2201-2212, <https://doi.org/10.1080/02678292.2019.1614685>.
- [6] A. Deptuch, M. Jasiurkowska-Delaporte, W. Zajęc, E. Juszyńska-Gałązka, A. Drzewicz, M. Urbańska, Investigation of crystallization kinetics and its relationship with molecular dynamics for chiral fluorinated glassforming smectogen 3F5HPHF6, *Phys. Chem. Chem. Phys.* 23 (2021) 19795-19810, <https://doi.org/10.1039/D1CP02297K>.
- [7] D. Demus, J. Goodby, G.W. Gray, H.-W. Spiess, V. Vill (Eds.), *Handbook of Liquid Crystals*, WILEY-VCH Verlag GmbH, Weinheim 1998.
- [8] N.A. Clark, S.T. Lagerwall, Submicrosecond bistable electro-optic switching in liquid crystals, *Appl. Phys. Lett.* 36 (1980) 899-901, <https://doi.org/10.1063/1.91359>.
- [9] J.T. Mills, H.F. Gleeson, J.W. Goodby, M. Hird, A. Seed, P. Styring, X-ray and optical studies of the tilted phases of materials exhibiting antiferroelectric, ferrielectric and ferroelectric mesophases, *J. Mater. Chem.* 8 (1998) 2385-2390, <https://doi.org/10.1039/A805611K>.
- [10] Y. Takanishi, K. Miyachi, S. Yoshida, B. Jin, H. Yin, K. Ishikawa, H. Takezoe, A. Fukuda, Stability of antiferroelectricity and molecular reorientation in the hexatic smectic  $I_A^*$  phase as studied by X-ray diffraction and NMR spectroscopy, *J. Mater. Chem.* 8 (1998) 1133-1138, <https://doi.org/10.1039/A707920F>.
- [11] W. Piecek, Z. Raszewski, P. Perkowski, J. Przedmojski, J. Kędzierski, W. Drzewiński, R. Dąbrowski, J. Zieliński, Apparent Tilt Angle and Structural Investigations of the Fluorinated Antiferroelectric Liquid Crystal Material for Display Application, *Ferroelectric* 310 (2004) 125-129, <https://doi.org/10.1080/00150190490510573>.

- [12] D. Ziobro, R. Dąbrowski, M. Tykarska, W. Drzewiński, M. Filipowicz, W. Rejmer, K. Kuśmierk, P. Morawiak, W. Piecek, Synthesis and properties of new ferroelectric and antiferroelectric liquid crystals with a biphenyl benzoate rigid core, *Liq. Cryst.* 39 (2012) 1011-1032, <https://doi.org/10.1080/02678292.2012.691560>.
- [13] N. Hu, R. Shao, C. Zhu, Y. Shen, C. Park, E. Korblova, C. Guerra, J.A. Rego, A. Hexemer, N.A. Clark, D.M. Walba, Ferroelectric and antiferroelectric odd–even behavior in a tricarbosilane-terminated liquid crystal homologous series, *Chem. Sci.* 5 (2014) 1869-1874, <https://doi.org/10.1039/c3sc53353k>.
- [14] P.S. Clegg, X-ray studies of the phases and phase transitions of liquid crystals, *Acta Cryst. A* 61 (2005) 112-121, <https://doi.org/10.1107/S0108767304025991>.
- [15] J.P.F. Lagerwall, F. Giesselmann, Current Topics in Smectic Liquid Crystal Research, *ChemPhysChem* 7 (2006) 20-45, <https://doi.org/10.1002/cphc.200500472>.
- [16] M. Urbańska, P. Morawiak, M. Senderek, Investigation of the tilt angle and spontaneous polarization of antiferroelectric liquid crystals with a chiral centre based on (S)-(+)-3-octanol, *J. Mol. Liq.* 328 (2021) 115378, <https://doi.org/10.1016/j.molliq.2021.115378>.
- [17] K. D'havé, P. Rudquist, S.T. Lagerwall, H. Pauwels, W. Drzewiński, R. Dąbrowski, Solution of the dark state problem in antiferroelectric liquid crystal displays, *Appl. Phys. Lett.* 76 (2000) 3528-3530, <https://doi.org/10.1063/1.126696>.
- [18] S. Lagerwall, A. Dahlgren, P. Jägemalm, P. Rudquist, K. D'havé, H. Pauwels, R. Dąbrowski, W. Drzewiński, Unique Electro-Optical Properties of Liquid Crystals Designed for Molecular Optics, *Adv. Funct. Mater.* 11 (2001) 87-94, [https://doi.org/10.1002/1616-3028\(200104\)11:2<87::AID-ADFM87>3.0.CO;2-E](https://doi.org/10.1002/1616-3028(200104)11:2<87::AID-ADFM87>3.0.CO;2-E).
- [19] R. Dąbrowski, J. Gałowska, J. Otón, W. Piecek, J. Przedmojski, M. Tykarska, High tilted antiferroelectric liquid crystalline materials, *Displays* 25 (2004) 9-19, <https://doi.org/10.1016/j.displa.2004.04.002>.
- [20] Ł. Kolek, M. Jasiurkowska-Delaporte, E. Juszyńska-Gałazka, Kinetics of non-isothermal cold crystallization in the antiferroelectric smectic phase of 3F5BFBiHex as seen by differential scanning calorimetry and broadband dielectric spectroscopy, *J. Mol. Liq.* 323 (2021) 115040, <https://doi.org/10.1016/j.molliq.2020.115040>.
- [21] A. Drzewicz, E. Juszyńska-Gałazka, M. Jasiurkowska-Delaporte, P. Kula, Insight into cold- and melt crystallization phenomena of a smectogenic liquid crystal, *CrystEngComm* 24 (2022) 3074-3087, <https://doi.org/10.1039/D2CE00224H>.
- [22] A. Drzewicz, Insight into phase situation and kinetics of cold- and melt crystallization processes of chiral smectogenic liquid crystals, Institute of Nuclear Physics Polish Academy of Sciences, Kraków 2023, <https://doi.org/10.48733/978-83-63542-37-5>.
- [23] A. Deptuch, M. Jasiurkowska-Delaporte, E. Juszyńska-Gałazka, A. Drzewicz, M. Urbańska, Phase Sequence, Kinetics of Crystallization and Molecular Dynamics of the Chiral Liquid Crystalline Compound Forming a Hexatic Smectic Glass, *Crystals* 12 (2022) 1583, <https://doi.org/10.3390/cryst12111583>.
- [24] S. Puupponen, A. Seppälä, Cold-crystallization of polyelectrolyte absorbed polyol for long-term thermal energy storage, *Sol. Energy Mater. Sol. Cells* 180 (2018) 59-66, <https://doi.org/10.1016/j.solmat.2018.02.013>.
- [25] T. Ishikawa, A. Honda, K. Miyamura, Effects of alkyl chain length on the cold crystallization of Schiff-base nickel(II) complexes, *CrystEngComm* 24 (2022) 5900-5906, <https://doi.org/10.1039/D2CE00305H>.
- [26] T. Roisnel, J. Rodriguez-Carvajal, WinPLOTR: a Windows tool for powder diffraction patterns analysis, *Materials Science Forum* 378-381 (2000) 118-123, <https://doi.org/10.4028/www.scientific.net/MSF.378-381.118>.
- [27] Origin Help. 17.7.3.6 Algorithms (K-Means Cluster Analysis), <https://www.originlab.com/doc/Origin-Help/KCA-Algorithm>. Access: June 2024.
- [28] Gaussian 16, Revision C.01, M. J. Frisch, G. W. Trucks, H. B. Schlegel, G. E. Scuseria, M. A. Robb, J. R. Cheeseman, G. Scalmani, V. Barone, G. A. Petersson, H. Nakatsuji, X. Li, M. Caricato, A. V. Marenich, J. Bloino, B. G. Janesko, R. Gomperts, B. Mennucci, H. P. Hratchian, J. V. Ortiz, A. F. Izmaylov, J. L. Sonnenberg, D. Williams-Young, F. Ding, F. Lipparini, F. Egidi, J. Goings, B. Peng, A. Petrone, T. Henderson, D. Ranasinghe, V. G. Zakrzewski, J. Gao, N. Rega, G. Zheng, W. Liang, M. Hada, M. Ehara, K. Toyota, R. Fukuda, J. Hasegawa, M. Ishida, T. Nakajima, Y. Honda, O. Kitao, H. Nakai, T. Vreven, K. Throssell, J. A. Montgomery, Jr., J. E. Peralta, F. Ogliaro, M. J. Bearpark, J. J. Heyd, E. N. Brothers, K.

N. Kudin, V. N. Staroverov, T. A. Keith, R. Kobayashi, J. Normand, K. Raghavachari, A. P. Rendell, J. C. Burant, S. S. Iyengar, J. Tomasi, M. Cossi, J. M. Millam, M. Klene, C. Adamo, R. Cammi, J. W. Ochterski, R. L. Martin, K. Morokuma, O. Farkas, J. B. Foresman, and D. J. Fox, Gaussian, Inc., Wallingford CT, 2019.

[29] F. Weigend, R. Ahlrichs, Balanced basis sets of split valence, triple zeta valence and quadruple zeta valence quality for H to Rn: design and assessment of accuracy, *Phys. Chem. Chem. Phys.* 7 (2005) 3297-3305, <https://doi.org/10.1039/B508541A>.

[30] C. Lee, W. Yang, R.G. Parr, Development of the Colle-Salvetti correlation-energy formula into a functional of the electron density, *Phys. Rev. B*, 37 (1988) 785-789, <https://doi.org/10.1103/PhysRevB.37.785>.

[31] A.D. Becke, Density-functional thermochemistry. III. The role of exact exchange, *J. Chem. Phys.* 98 (1993) 5648-5652, <https://doi.org/10.1063/1.464913>.

[32] S. Grimme, J. Antony, S. Ehrlich, H. Kries, A consistent and accurate ab initio parametrization of density functional dispersion correction (DFT-D) for the 94 elements H-Pu, *J. Chem. Phys.* 132 (2010), 154104, <https://doi.org/10.1063/1.3382344>.

[33] S. Grimme, S. Ehrlich, L. Goerigk, Effect of the damping function in dispersion corrected density functional theory, *J. Comput. Chem.* 32 (2011) 1456-1465, <https://doi.org/10.1002/jcc.21759>.

[34] M.D. Hanwell, D.E. Curtis, D.C. Lonie, T. Vandermeersch, E. Zurek, G. R. Hutchison, Avogadro: an advanced semantic chemical editor, visualization, and analysis platform, *J. Cheminf.* 4 (2012) 17, <https://doi.org/10.1186/1758-2946-4-17>.

[35] W. Massa, Crystal Structure Determination, Springer-Verlag, Berlin Heidelberg 2000, <https://doi.org/10.1007/978-3-662-04248-9>.

[36] R. Puertas, M.A. Rute, J. Salud, D.O. López, S. Diez, J. Kees van Miltenburg, L.C. Pardo, J.Ll. Tamarit, M. Barrio, M.A. Pérez-Jubindo, M.R. de la Fuente, Thermodynamic, crystallographic, and dielectric study of the nature of glass transitions in cyclo-octanol, *Phys. Rev. B* 69 (2004) 224202, <https://doi.org/10.1103/PhysRevB.69.224202>.

[37] N. Podoliak, V. Novotná, M. Glogarová, V. Hamplová, M. Kašpar, A. Bubnov, N. Kapernaum, F. Giesselmann, Study of de Vries behaviour of the smectic A\*-smectic C\* phase transition, *Phase Trans.* 83 (2010) 1026-1036, <https://doi.org/10.1080/01411594.2010.509615>.

[38] J. Chruściel, A. Rudzki, M.D. Ossowska-Chruściel, S. Zalewski, Studies of de Vries SmA\* type phase in chiral thiobenzoates, *Phase Trans.* 96 (2023) 157-165, <https://doi.org/10.1080/01411594.2022.2159403>.

[39] B.B. He, Section 2.5.3.3.4. Lorentz, polarization and absorption corrections, in C.J. Gilmore, J.A. Kaduk, H. Schenk, *International Tables for Crystallography, Volume B* (2019) 130-131.

[40] J. Budai, R. Pindak, S.C. Davey, J.W. Goodby, A structural investigation of the liquid crystal phases of 4-(2'-methylbutyl)phenyl 4'-n-octylbiphenyl-4-carboxylate, *J. Phys. Lett.* 45 (1984) 1053-1062, <https://doi.org/10.1051/jphyslet:0198400450210105300>.

[41] W. Tomczyk, M. Marzec, E. Juszyńska-Gałazka, D. Węglowska, Mesomorphic and physicochemical properties of liquid crystal mixture composed of chiral molecules with perfluorinated terminal chains, *J. Mol. Struct.* 1130 (2017) 503-510, <https://doi.org/10.1016/j.molstruc.2016.10.039>.

[42] K.Ch. Dey, P.Kr. Mandal, P. Kula, Effect of fluorinated achiral chain length on structural, dielectric and electro-optic properties of two terphenyl based antiferroelectric liquid crystals, *J. Mol. Liq.* 298 (2020) 112056, <https://doi.org/10.1016/j.molliq.2019.112056>.

[43] Y. Ouchi, Y. Yoshioka, H. Ishii, K. Seki, M. Kitamura, R. Noyori, Y. Takanishi, I. Nishiyama, Effect of the terminal branching structure of some liquid-crystalline biphenyl carboxylates on the stability of the antiferroelectric phase, *J. Mater. Chem.* 5 (1995) 2297-2304, <https://doi.org/10.1039/JM9950502297>.

[44] A. Bubnov, V. Novotná, V. Hamplová, M. Kašpar, M. Glogarová, Effect of multilactate chiral part of liquid crystalline molecule on mesomorphic behavior, *J. Mol. Struct.* 892 (2008) 151-157, <https://doi.org/10.1016/j.molstruc.2008.05.016>.

- [45] A. Resetic, J. Milavec, A. Bubnov, D. Pocięcha, V. Hamplova, E. Górecka, B. Zalar, V. Domenici, New Liquid Crystalline Elastomeric Films Containing a Smectic Crosslinker: Chemical and Physical Properties, *Crystals* 13 (2023) 96, <https://doi.org/10.3390/cryst13010096>.
- [46] K. El Guermai, M. Ayadi, K. El Boussiri, Correlation Length in PBnA Liquid Crystal Family, *Acta Phys. Pol. A* 94 (1998) 779-784, <http://dx.doi.org/10.12693/APhysPolA.94.779>.
- [47] B.M. Ocko, A.R. Kortan, R.J. Birgeneau, J.W. Goodby, A high resolution X-ray scattering study of the phases and phase transitions in N-(4-n-butyloxybenzylidene)-4-n-heptylaniline (40.7), *J. Phys.* 45 (1984) 113-128, <https://doi.org/10.1051/jphys:01984004501011300>.
- [48] A. Deptuch, A. Lelito, B. Sęk, M. Urbańska, Comparative X-ray diffraction study of two liquid crystalline compounds with the chiral centers based on (S)-(+)-2-octanol and (S)-(+)-3-octanol, *Acta Phys. Pol. A* 146 (2024) 79-86, <http://doi.org/10.12693/APhysPolA.146.79>.
- [49] W. Piecek, Z. Raszewski, P. Perkowski, J. Kędzierski, J. Rutkowska, J. Zieliński, E. Nowinowski-Kruszelnicki, R. Dąbrowski, M. Tykarska, J. Przedmojski, The Origin of High Optical Tilt in a Homologous Series of Fluorinated Antiferroelectric Liquid Crystals, *Mol. Cryst. Liq. Cryst.* 436 (2005) 149/[1103]-165/[1119], <https://doi.org/10.1080/15421400590955578>.
- [50] W. Piecek, P. Perkowski, Z. Raszewski, P. Morawiak, M. Żurowska, R. Dąbrowski, K. Czupryński, Long Pitch Orthoconic Antiferroelectric Binary Mixture for Display Applications, *Mol. Cryst. Liq. Cryst.* 525 (2010) 140-152, <https://doi.org/10.1080/15421401003796223>.
- [51] R.S. Rowland, R. Taylor, Intermolecular Nonbonded Contact Distances in Organic Crystal Structures: Comparison with Distances Expected from van der Waals Radii, *J. Phys. Chem.* 100 (1996) 7384-7391, <https://doi.org/10.1021/jp953141+>.
- [52] J.C. Zapata Trujillo, L.K. McKemmish, Model Chemistry Recommendations for Scaled Harmonic Frequency Calculations: A Benchmark Study, *J. Phys. Chem. A* 127 (2023) 1715-1735, <https://doi.org/10.1021/acs.jpca.2c06908>.
- [53] K. Drużbicki, A. Kocot, E. Mikuli, M.D. Ossowska-Chruściel, J. Chruściel, Temperature-Dependent Infrared Spectroscopy Studies of a Novel Antiferroelectric Liquid-Crystalline Thiobenzoate, *J. Phys. Chem. B* 116 (2012) 11332-11343, <https://doi.org/10.1021/jp305099v>.
- [54] R. Chaudhary, A. Yadav, A.S. Bahota, N. Agrawal, V. Prasad, B.S. Araújo, A.P. Ayala, S. Singh, P. Tandon, Unraveled mesophase dynamics of discotic liquid crystal using combination of vibrational spectroscopy and DFT, *J. Mol. Liq.* 397 (2024) 124076, <https://doi.org/10.1016/j.molliq.2024.124076>.
- [55] I. Łukaszewska, S. Lalik, A. Bukowczan, M. Marzec, K. Pielichowski, K.N. Raftopoulos, Tailoring the physical properties of non-isocyanate polyurethanes by introducing secondary amino groups along their main chain, *J. Mol. Liq.* 391 (2023) 123263, <https://doi.org/10.1016/j.molliq.2023.123263>.
- [56] C. Wang, P. Li, S. Zhang, G. Zhang, S. Tan, Y. Wu, M. Watanabe, Azobenzene Molecular Trigger Controlling Phase Transitions of PNIPAm in Ionic Liquids and Light-Controlled Adhesiveness, *Macromolecules* 53 (2020) 4901-4907, <https://doi.org/10.1021/acs.macromol.0c00652>.
- [57] K. Drużbicki, E. Mikuli, M.D. Ossowska-Chruściel, Experimental (FT-IR, FT-RS) and theoretical (DFT) studies of vibrational dynamics and molecular structure of 4-n-pentylphenyl-4'-n-octyloxythiobenzoate (8OS5), *Vib. Spectrosc.* 52 (2010) 54-62, <https://doi.org/10.1016/j.vibspec.2009.10.003>.
- [58] A. Drzewicz, A. Bombalska, M. Tykarska, Impact of molecular structure of smectogenic chiral esters (3FmX<sub>1</sub>X<sub>2</sub>r) on vibrational dynamics as seen by IR and Raman spectroscopy, *Liq. Cryst.* 46 (2019) 754-771, <https://doi.org/10.1080/02678292.2018.1527959>.
- [59] R. Gautam, S. Vanga, F. Ariese, S. Umopathy, Review of multidimensional data processing approaches for Raman and infrared spectroscopy, *EPJ Tech. Instrum.* 2 (2015) 8, <https://doi.org/10.1140/epjti/s40485-015-0018-6>.
- [60] C. Yuan, H. Yang, Research on K-Value Selection Method of K-Means Clustering Algorithm, *J* 2 (2019) 226-235, <https://doi.org/10.3390/j2020016>.

- [61] N. Osiecka-Drewniak, M.A. Czarnecki, Z. Galewski, Investigation of phase transitions in liquid crystal 12BBAA using window clustering of infrared spectra, *J. Mol. Liq.* 341 (2021) 117233, <https://doi.org/10.1016/j.molliq.2021.117233>.
- [62] N. Osiecka-Drewniak, E. Juszyńska-Gałązka, W. Zając, D. Chudoba, Vibrational dynamics of ethosuximide polymorphs. Infrared absorption and inelastic neutron scattering spectroscopy and model calculations, *Spectrochim. Acta A Mol. Biomol. Spectrosc.* 279 (2022) 121468, <https://doi.org/10.1016/j.saa.2022.121468>.
- [63] K. Ema, H. Yao, I. Kawamura, T. Chan, C.W. Garland, High-resolution calorimetric study of the antiferroelectric liquid crystals methylheptyloxycarbonylphenyl octyloxybiphenyl carboxylate and its octylcarbonylbiphenyl analog, *Phys. Rev. E* 47 (1993) 1203-1211, <https://doi.org/10.1103/PhysRevE.47.1203>.

# Structural and dynamical investigation of glassforming smectogen by X-ray diffraction and infra-red spectroscopy aided by density functional theory calculations

Aleksandra Deptuch<sup>1,\*</sup>, Natalia Górka<sup>2</sup>, Stanisław Baran<sup>3</sup>, Magdalena Urbańska<sup>4</sup>

<sup>1</sup> Institute of Nuclear Physics Polish Academy of Sciences, Radzikowskiego 152, PL-31342 Kraków, Poland

<sup>2</sup> Faculty of Chemistry, Jagiellonian University, Gronostajowa 2, PL-30387 Kraków, Poland

<sup>3</sup> Jagiellonian University, Faculty of Physics, Astronomy and Applied Computer Science, M. Smoluchowski Institute of Physics, Łojasiewicza 11, PL-30-348 Kraków, Poland

<sup>4</sup> Institute of Chemistry, Military University of Technology, Kaliskiego 2, PL-00908 Warsaw, Poland

\*corresponding author, [aleksandra.deptuch@ifj.edu.pl](mailto:aleksandra.deptuch@ifj.edu.pl)

## Electronic Supplementary Information

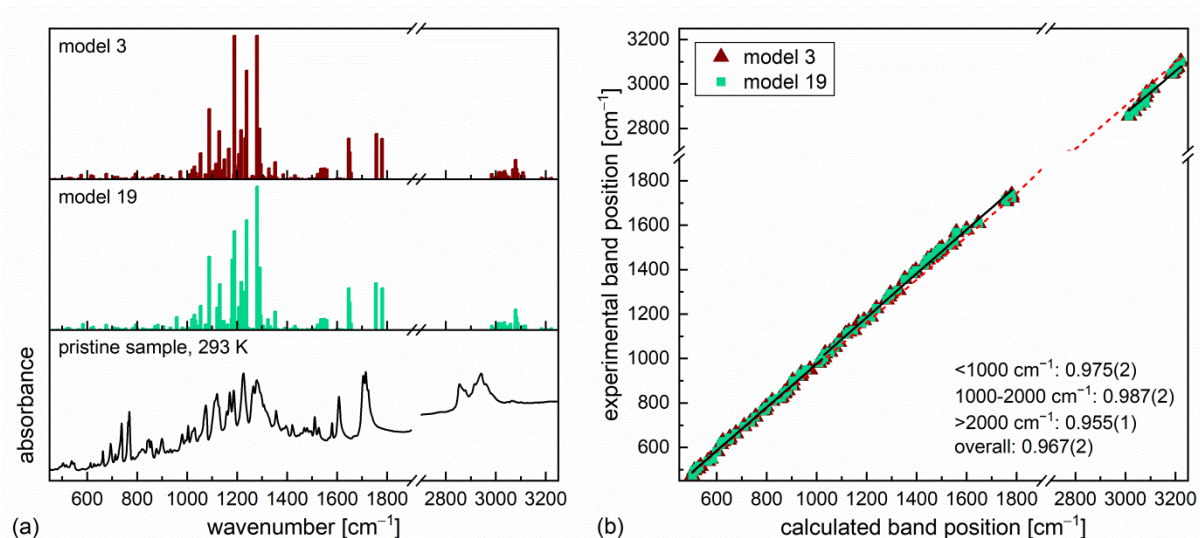


Figure S1. IR spectrum of 7HH6 collected for the pristine sample at 293 K compared to the unscaled calculated spectra for molecular models 3 and 19 (DFT, def2TZVPP basis set, B3LYP-D3(BJ) functional) (a) and scaling between the calculated and experimental band positions (b). The overall scaling factor is equal to 0.967(2). The scaling factors calculated separately for  $>1000$  cm<sup>-1</sup>, 1000-2000 cm<sup>-1</sup> and  $>2000$  cm<sup>-1</sup>, are equal to 0.975(2), 0.987(2) and 0.955(1), respectively.

Table S1. The band assignment of the experimental IR spectra of 7HH6 measured for the pristine sample at 293 K, based on the DFT calculations (def2TZVPP basis set, B3LYP-D3(BJ) functional). Experimental and calculated band positions are given in  $\text{cm}^{-1}$ . The intra-molecular vibrations are denoted as follows:  $\beta$  – in-plane deformation,  $\gamma$  – out-of-plane deformation,  $\delta$  – scissoring,  $\nu$  – stretching,  $\rho$  – rocking,  $\tau$  – twisting,  $\omega$  – wagging.

experimental	model 3	model 19	interpretation
475	502.1	503.7	$\rho\text{CF}_2(\text{a}), \delta\text{CCC}(\text{c})$
496	510.4	511.0	$\gamma\text{Ph}(\text{d},\text{f},\text{g}), \delta\text{CCC}(\text{j})$
504	526.1	521.8	$\delta\text{CF}_2(\text{a}), \rho\text{CH}_2(\text{b})^{\text{model3}}, \gamma\text{Ph}(\text{d})^{\text{model19}}$
516	535.8	529.5	$\delta\text{CF}_2(\text{a}), \delta\text{COC}(\text{b},\text{c}), \delta\text{CCC}(\text{c}), \gamma\text{Ph}(\text{f},\text{g}), \delta\text{OCC}(\text{b},\text{c})^{\text{model3}}, \beta_{\text{asym}}\text{Ph}(\text{d})^{\text{model3}}, \gamma\text{Ph}(\text{d})^{\text{model19}}$
538	565.4	565.1	$\gamma\text{Ph}(\text{f},\text{g})$
548	576.2	584.0	$\delta\text{CF}_2(\text{a}), \delta\text{CCO}(\text{a},\text{b})$
582	602.4	600.5	$\rho\text{CF}_2(\text{a}), \rho\text{CH}_2(\text{b})$
614	616.6	617.3	$\delta\text{CF}_2(\text{a}), \rho\text{CH}_2(\text{b})$
627	624.7	624.7	$\beta_{\text{asym}}\text{Ph}(\text{d},\text{f},\text{g})$
634	648.7	648.8	$\beta_{\text{asym}}\text{Ph}(\text{d},\text{g}), \gamma\text{Ph}(\text{f})$
643	651.9	651.9	$\beta_{\text{asym}}\text{Ph}(\text{d},\text{f},\text{g})$
663	677.3	677.1	$\beta_{\text{asym}}\text{Ph}(\text{d},\text{g}), \gamma\text{Ph}(\text{f})$
695	709.9	710.0	$\gamma\text{Ph}(\text{d})$
714	735.6	735.9	$\rho\text{CH}_2(\text{j})$
738	755.7	754.4	$\rho\text{CH}_2(\text{c})$
765	783.5	783.4	$\gamma\text{Ph}(\text{d})$
769	793.8	795.2	$\gamma\text{Ph}(\text{d},\text{f},\text{g}), \rho\text{CH}_2(\text{j})$
783	798.4	800.7	$\rho\text{CH}_2(\text{j})$
809	822.7	822.9	$\gamma\text{Ph}(\text{f},\text{g})$
820	853.6	844.2	$\tau\text{CH}_2(\text{j})^{\text{model3}}, \gamma\text{Ph}(\text{f})^{\text{model19}}$
826	859.6	860.0	$\gamma\text{Ph}(\text{f},\text{g})$
843	869.5	869.6	$\gamma\text{Ph}(\text{d},\text{f},\text{g})$
847	872.6	872.7	$\gamma\text{Ph}(\text{d})$
856	883.1	883.6	$\gamma\text{Ph}(\text{f},\text{g})$
878	904.1	904.5	$\nu\text{CC}(\text{a},\text{b})^{\text{model3}}, \rho\text{CH}_2(\text{b})^{\text{model3}}, \gamma\text{Ph}(\text{f},\text{g})^{\text{model19}}$
900	904.2	906.0	$\gamma\text{Ph}(\text{f},\text{g})^{\text{model3}}, \nu\text{CC}(\text{a},\text{b})^{\text{model19}}, \rho\text{CH}_2(\text{b})^{\text{model19}}$
921	935.8	932.9	$\nu_{\text{asym}}\text{OC}^*\text{C}(\text{h},\text{i},\text{j})$
933	938.8	938.7	$\tau\text{CH}_2(\text{c}), \rho\text{CH}_2(\text{c})$
950	973.7	959.1	$\nu_{\text{sym}}\text{COC}(\text{b},\text{c}), \nu_{\text{sym}}\text{CCC}(\text{c})$
980	1010.1	1009.8	$\rho\text{CH}_2(\text{b}), \nu_{\text{sym}}\text{CCC}(\text{c})$
995	1021.7	1020.8	$\rho\text{CH}_2(\text{b}), \nu_{\text{sym}}\text{CCC}(\text{c})$
1005	1029.8	1029.7	$\beta_{\text{asym}}\text{Ph}(\text{d})$
1023	1033.8	1033.6	$\beta_{\text{asym}}\text{Ph}(\text{d},\text{f},\text{g})$
1029	1054.4	1054.6	$\nu_{\text{asym}}\text{CCC}(\text{c}), \nu\text{CO}(\text{c}), \beta_{\text{asym}}\text{Ph}(\text{d},\text{f},\text{g})$
1051	1073.5	1073.5	$\nu_{\text{asym}}\text{CCC}(\text{c}), \nu_{\text{sym}}\text{CCC}(\text{c})$
1074	1089.4	1089.3	$\beta_{\text{asym}}\text{Ph}(\text{d},\text{f}), \nu\text{CO}(\text{e})$
1111	1115.6	1121.2	$\nu_{\text{sym}}\text{CF}_2(\text{a}), \tau\text{CH}_2(\text{b})$
1120	1129.3	1131.6	$\beta_{\text{asym}}\text{Ph}(\text{g}), \nu_{\text{asym}}\text{COC}(\text{h},\text{i})$
1127	1149.8	1147.9	$\nu_{\text{asym}}\text{CF}_2(\text{a}), \nu_{\text{sym}}\text{CCC}(\text{c}), \beta_{\text{sym}}\text{Ph}(\text{d}), \nu_{\text{asym}}\text{COC}(\text{b},\text{c})^{\text{model3}}, \rho\text{CH}_2(\text{b})^{\text{model19}}$
1159	1167.1	1181.5	$\nu_{\text{asym}}\text{CF}_2(\text{a}), \rho\text{CH}_2(\text{b}), \nu_{\text{asym}}\text{COC}(\text{b},\text{c})^{\text{model19}}$
1171	1189.5	1189.5	$\beta_{\text{sym}}\text{Ph}(\text{d},\text{f})$
1187	1216.6	1217.8	$\omega\text{CF}_2(\text{a}), \omega\text{CH}_2(\text{b})$
1225	1238.5	1238.5	$\beta_{\text{sym}}\text{Ph}(\text{d},\text{g}), \beta_{\text{asym}}\text{Ph}(\text{f}), \nu_{\text{asym}}\text{COC}(\text{e},\text{f})$
1265	1280.4	1280.5	$\beta_{\text{asym}}\text{Ph}(\text{d},\text{f}), \nu_{\text{asym}}\text{CCO}(\text{d},\text{e})$
1279	1290.7	1291.7	$\beta_{\text{asym}}\text{Ph}(\text{g}), \nu_{\text{asym}}\text{CCO}(\text{g},\text{h}), \delta\text{OC}^*\text{H}(\text{h},\text{i})$
1292	1295.5	1295.5	$\omega\text{CH}_2(\text{c}), \beta_{\text{asym}}\text{Ph}(\text{d}), \nu_{\text{asym}}\text{CCO}(\text{d},\text{e})$



Table S1 (continuation).

1307	1327.7	1323.9	$\omega\text{CF}_2(\text{a}), \tau\text{CH}_2(\text{b,c})$
1357	1352.6	1353.0	$\tau\text{CH}_2(\text{b}), \omega\text{CH}_2(\text{c}), \beta_{\text{asym}}\text{Ph}(\text{d}), \tau\text{CH}_2(\text{c})^{\text{model19}}$
1384	1385.1	1385.1	$\omega\text{CH}_2(\text{i,j})$
1396	1397.3	1397.5	$\omega\text{CH}_2(\text{b,c})$
1422	1432.0	1432.3	$\omega\text{CH}_2(\text{c}), \beta_{\text{asym}}\text{Ph}(\text{d})$
1445	1444.5	1443.0	$\omega\text{CH}_2(\text{b,c})$
1457	1459.8	1459.7	$\beta_{\text{asym}}\text{Ph}(\text{d,f,g})$
1469	1477.9	1478.2	$\delta\text{CH}_2(\text{i,j})^{\text{model13}}, \delta\text{CH}_2(\text{b,c})^{\text{model19}}, \omega\text{CH}_2(\text{c})^{\text{model19}}$
1480	1488.2	1484.3	$\delta\text{CH}_2(\text{b,c})^{\text{model13}}, \omega\text{CH}_2(\text{c})^{\text{model13}}, \delta\text{CH}_2(\text{i,j})^{\text{model19}}$
1490	1491.8	1494.5	$\delta\text{CH}_2(\text{i,j})$
1496	1501.1	1501.1	$\delta\text{CH}_3(\text{j})$
1511	1536.4	1536.5	$\beta_{\text{asym}}\text{Ph}(\text{f,g})$
1527	1550.0	1550.1	$\beta_{\text{asym}}\text{Ph}(\text{d})$
1568	1559.3	1559.3	$\beta_{\text{asym}}\text{Ph}(\text{f,g})$
1580	1600.3	1600.3	$\beta_{\text{asym}}\text{Ph}(\text{f,g})$
1608	1647.5	1647.5	$\beta_{\text{sym}}\text{Ph}(\text{d,f,g})$
1706	1758.2	1756.1	$\nu\text{C}=\text{O}(\text{h})$
1716	1758.2	1756.1	$\nu\text{C}=\text{O}(\text{h})$
1724	1780.8	1781.2	$\nu\text{C}=\text{O}(\text{e})$
1736	1780.8	1781.2	$\nu\text{C}=\text{O}(\text{e})$
2856	3014.7	3014.4	$\nu_{\text{sym}}\text{CH}_2(\text{c}), \nu_{\text{asym}}\text{CH}_2(\text{j})$
2877	3035.5	3034.9	$\nu_{\text{sym}}\text{CH}_2(\text{c}), \nu_{\text{sym}}\text{CH}_2(\text{b})^{\text{model13}}, \nu_{\text{asym}}\text{CH}_2(\text{c})^{\text{model19}}$
2901	3053.3	3053.4	$\nu_{\text{asym}}\text{CH}_2(\text{c})$
2915	3069.5	3078.1	$\nu_{\text{asym}}\text{CH}(\text{i,j})$
2941	3079.5	3079.4	$\nu_{\text{asym}}\text{CH}_2(\text{c})$
2959	3083.7	3083.3	$\nu_{\text{asym}}\text{CH}_2(\text{j})$
2981	3109.1	3110.0	$\nu\text{CH}_3(\text{i})$
3046	3183.6	3183.6	$\nu_{\text{asym}}\text{CH}(\text{f,g})$
3049	3189.9	3190.0	$\nu_{\text{asym}}\text{CH}(\text{f,g})$
3065	3196.4	3196.4	$\nu_{\text{asym}}\text{CH}(\text{d})$
3072	3202.8	3202.9	$\nu_{\text{sym}}\text{CH}(\text{f}), \nu_{\text{asym}}\text{CH}(\text{d,g})$
3076	3208.1	3207.6	$\nu_{\text{sym}}\text{CH}(\text{f,g})$
3100	3221.8	3222.3	$\nu_{\text{sym}}\text{CH}(\text{d})$

Table S2. Atomic coordinates of the molecular models 3 and 19 of 7HH6 optimized by the DFT method (def2TZVPP basis set, B3LYP-D3(BJ) functional).

atom	model 3			model 19		
	x	y	z	x	y	z
C	13.48027	-0.39029	-1.14851	14.15474	-2.46000	-1.39879
C	12.25471	-0.05772	-1.70331	13.22369	-2.54803	-2.42131
C	11.20606	-0.96247	-1.63815	12.21560	-3.49731	-2.34865
C	11.36263	-2.20340	-1.01452	12.11842	-4.36320	-1.25589
C	12.61158	-2.50999	-0.46402	13.07310	-4.24963	-0.23967
C	13.66936	-1.61733	-0.52937	14.08939	-3.31009	-0.30441
H	12.13157	0.90728	-2.17405	13.29275	-1.86944	-3.25960
H	10.24592	-0.68907	-2.05265	11.47881	-3.54692	-3.13804
H	12.76636	-3.47332	0.00140	13.03557	-4.92425	0.60415
H	14.62869	-1.86801	-0.10422	14.82190	-3.23557	0.48424
C	9.34205	-3.30400	-2.00078	10.59195	-6.03733	-2.32101
C	10.24279	-3.16248	-0.93840	11.03995	-5.36828	-1.17571
C	10.05091	-3.95422	0.19928	10.43563	-5.67750	0.04794
C	8.29113	-4.20066	-1.92849	9.57975	-6.97734	-2.24631
H	9.48433	-2.72158	-2.90041	11.06073	-5.83396	-3.27374
C	8.10932	-4.98511	-0.78964	8.98522	-7.27864	-1.02115
H	7.60108	-4.31500	-2.75188	9.23984	-7.49872	-3.12946
C	9.00055	-4.85342	0.27553	9.42329	-6.61895	0.12741
H	10.71800	-3.84343	1.04277	10.74622	-5.15435	0.94158
H	8.86003	-5.45021	1.16368	8.96083	-6.84034	1.07718
C	6.96139	-5.92899	-0.76050	7.89925	-8.29275	-0.99448
O	6.17266	-6.05769	-1.66769	7.48792	-8.86947	-1.97490
O	6.90449	-6.61809	0.39450	7.42544	-8.49724	0.24761
C	5.80740	-7.55063	0.59613	6.32684	-9.43800	0.40442
C	4.88256	-6.97513	1.65845	5.00466	-8.74656	0.08204
C	6.42209	-8.87983	0.98908	6.43594	-9.97391	1.81834
H	5.27812	-7.63877	-0.35081	6.48388	-10.23962	-0.31591
H	6.99563	-8.78269	1.91180	6.37861	-9.17107	2.55205
H	7.08600	-9.24446	0.20603	7.38194	-10.49597	1.95661
H	5.63884	-9.62161	1.14797	5.62402	-10.67546	2.01229
C	4.23880	-5.64694	1.27202	4.67737	-7.53045	0.94548
H	5.44540	-6.85978	2.58980	4.21099	-9.49358	0.17668
H	4.10304	-7.71705	1.85487	5.02684	-8.45471	-0.96930
C	3.29017	-5.11254	2.34116	3.40168	-6.82164	0.49804
H	3.69973	-5.76530	0.32807	5.51274	-6.82680	0.91004
H	5.01972	-4.90601	1.08453	4.57038	-7.82823	1.99187
C	2.65308	-3.77700	1.96843	3.05895	-5.60084	1.34675
H	3.83351	-5.00255	3.28558	2.56474	-7.52744	0.52454
H	2.50196	-5.84910	2.52968	3.50694	-6.51714	-0.54815
C	1.70335	-3.23573	3.03401	1.78702	-4.88478	0.89947
H	2.11108	-3.88621	1.02333	3.89711	-4.89657	1.32122
H	3.44158	-3.04099	1.78010	2.95215	-5.90515	2.39341
C	1.07305	-1.89994	2.65039	1.45497	-3.66505	1.75425
H	0.49780	-1.98881	1.72652	2.26234	-2.93065	1.71990
H	1.83796	-1.13762	2.48873	1.31079	-3.94598	2.79961
H	0.39977	-1.53572	3.42750	0.54318	-3.17252	1.41384
H	2.24660	-3.12707	3.97755	0.95025	-5.58926	0.92512
H	0.91602	-3.97215	3.22112	1.89510	-4.58126	-0.14604
C	16.29547	1.88753	-0.60876	16.59578	0.22584	-0.91917
C	17.09176	2.42901	0.39814	16.96236	1.22797	-0.02336
C	18.11372	3.31697	0.10311	18.03813	2.06178	-0.28286
H	16.89740	2.14313	1.42188	16.38910	1.34542	0.88501
C	18.35121	3.67556	-1.22660	18.76909	1.89511	-1.46229
H	18.71392	3.72066	0.90294	18.29900	2.82914	0.42850
C	17.55650	3.13521	-2.24393	18.40735	0.89071	-2.36721
C	16.54180	2.25313	-1.93782	17.33422	0.06761	-2.09832
H	17.75775	3.42560	-3.26521	18.98639	0.77907	-3.27278
H	15.93191	1.83993	-2.72646	17.06000	-0.70541	-2.79967
O	19.31879	4.53114	-1.62443	19.83363	2.65038	-1.81269
C	20.16785	5.12472	-0.64272	20.26422	3.69245	-0.93757
C	21.14566	6.03368	-1.35661	21.46444	4.36711	-1.56697

H	20.69721	4.34026	-0.09281	20.52434	3.26848	0.03739
H	19.56226	5.69102	0.07180	19.44921	4.40806	-0.79033
C	22.10383	6.72144	-0.38753	22.00482	5.50282	-0.70187
H	20.58404	6.78090	-1.92198	21.17976	4.74776	-2.55058
H	21.70785	5.44468	-2.08485	22.24309	3.61890	-1.73204
C	23.09579	7.64554	-1.08841	23.21793	6.19373	-1.31849
H	22.65524	5.96563	0.18080	22.27495	5.11455	0.28532
H	21.53141	7.29756	0.34654	21.21561	6.24247	-0.53315
C	24.05851	8.33631	-0.12659	23.76672	7.32866	-0.45832
H	22.54607	8.40237	-1.65628	22.94958	6.58379	-2.30506
H	23.66864	7.07128	-1.82278	24.00715	5.45506	-1.48822
O	26.87310	10.77554	-0.62040	26.66455	9.68483	-0.86281
C	27.87583	11.41376	0.11610	27.17984	10.85525	-0.30537
C	29.27103	10.86672	-0.18934	28.04598	10.64876	0.93920
H	27.70967	11.35955	1.19381	26.39392	11.56002	-0.00798
H	27.92075	12.46685	-0.17232	27.80603	11.32787	-1.05989
C	29.52011	9.39026	0.22097	29.15947	9.57586	0.77864
F	30.16980	11.64153	0.48662	27.28488	10.29951	2.01277
F	29.53850	10.98264	-1.51201	28.63522	11.84205	1.23552
C	31.00061	8.90442	0.18086	30.28687	9.60526	1.85476
F	28.80854	8.57763	-0.58756	29.75383	9.74227	-0.42489
F	29.08177	9.21635	1.49410	28.59797	8.34985	0.82055
F	31.02771	7.58801	0.41838	31.06462	8.52905	1.69910
F	31.73300	9.51366	1.11320	29.76780	9.58020	3.08490
F	31.54355	9.13127	-1.01594	31.04615	10.69368	1.72689
C	15.22561	0.94879	-0.21978	15.44090	-0.62563	-0.57525
O	14.51597	0.51890	-1.31160	15.18798	-1.54736	-1.55874
O	14.98281	0.59582	0.90450	14.78526	-0.53845	0.42974
C	25.04679	9.25849	-0.83580	24.98300	8.01038	-1.07974
H	24.60804	7.57753	0.43952	24.03227	6.93671	0.52850
H	23.48417	8.90921	0.60853	22.97697	8.06799	-0.29031
C	26.00055	9.92913	0.12894	25.52201	9.12657	-0.21050
H	24.50862	10.02890	-1.39303	24.72647	8.41650	-2.06104
H	25.63090	8.69248	-1.56491	25.77896	7.27935	-1.23974
H	26.57596	9.17778	0.67738	25.79592	8.74336	0.77563
H	25.45100	10.53233	0.86200	24.76828	9.91103	-0.06853

Table S3. Theoretical IR spectra for models 3 and 19 calculated by the DFT method (def2TZVPP basis set, B3LYP-D3(BJ) functional).

model 3		model 19	
wavenumber [cm <sup>-1</sup> ]	intensity	wavenumber [cm <sup>-1</sup> ]	intensity
3.385	0.0056939	3.406	0.00347898
4.0246	0.0102448	3.838	0.0113887
6.0017	0.011954	6.7639	0.0176028
9.1439	0.00642033	9.4861	0.00805198
10.6053	0.0155861	11.4963	0.00507625
11.6975	0.00521318	13.9184	0.0128875
17.067	0.0116549	17.9736	0.0109621
17.8812	0.0242071	18.8625	0.00749403
24.0242	0.00217928	26.5919	0.0044089
28.2331	0.0463311	28.6858	0.0245388
35.679	0.00799069	33.8561	0.00775659
41.4378	0.0466729	39.6805	0.0235761
43.2704	0.0393339	41.7493	0.0783427
46.0571	0.0975228	49.256	0.0478415
49.7723	0.0808256	53.0226	0.166214
53.4399	0.118685	57.1417	0.00495591
58.5035	0.0170497	62.3157	0.0631905
59.3322	0.00930467	62.6007	0.00904754
68.56	0.0127018	67.3864	0.00437608
71.8853	0.0346014	73.9649	0.015371
75.8697	0.0379985	77.1271	0.0211693
77.202	0.00664467	78.7037	0.0994463
85.9191	0.021013	83.2285	0.0213553
89.9985	0.0388211	83.9736	0.00588582
94.9966	0.0711577	100.837	0.0395707
109.002	0.0294203	105.955	0.0552917
110.259	0.0689144	116.275	0.0291337
115.14	0.0393125	120.263	0.0328425
124.427	0.0664894	123.546	0.010054
129.238	0.0218462	127.008	0.0474148
129.89	0.129133	138.049	0.171498
144.165	0.245799	145.525	0.043345
151.191	0.0426776	151.536	0.0418572
158.74	0.0226047	157.233	0.00506531
160.868	0.192311	165.878	0.0787584
168.144	0.228183	166.745	0.583156
169.787	0.0487347	171.344	0.21445
174.213	0.0344839	173.939	0.0274161
181.271	0.0520463	198.738	0.0326783
191.865	0.139218	200.416	0.294565
214.226	0.136568	206.822	0.121349
220.936	0.21858	221.157	0.139422
229.674	0.0711471	234.672	0.0732118
238.298	0.012189	240.06	0.015557
241.606	0.0354988	243.869	0.0642846
245.283	0.0541401	246.089	0.00510907
246.224	0.0117297	251.559	0.542338
257.168	0.61679	262.135	0.0681027
278.753	0.533443	279.211	0.63254
286.244	0.690105	286.538	0.885182
292.38	0.24096	292.88	0.0471194
297.044	0.655151	298.269	0.51595
305.262	0.225833	304.963	0.177603
314.973	0.147871	323.041	0.0760015
328.971	0.0919891	336.072	0.15872
341.96	0.12486	347.394	0.288099

---

350.81	0.463343	351.124	0.781228
363.033	0.199393	367.061	0.0657396
374.216	0.014379	373.9	0.0289368
386.922	0.193294	393.398	0.0727523
393.766	0.513423	394.494	0.752652
406.779	0.339733	405.01	0.170295
411.845	0.0912627	409.692	0.525457
421.465	0.0144217	418.329	0.379121
422.062	0.74353	421.47	0.0271536
428.297	0.0184811	428.308	0.0231057
429.612	0.00300185	429.724	0.00402599
436.372	0.516201	436.036	0.748375
457.425	0.0488735	443.559	0.407982
471.016	0.297354	461.286	0.083222
483.217	0.0933351	471.417	0.127639
499.82	0.690938	483.401	0.277662
502.121	0.455373	503.722	0.23354
510.442	0.547875	510.964	0.417773
519.46	0.405891	521.333	1.61402
522.29	0.686697	521.808	1.1542
526.145	1.09677	529.525	1.32779
533.678	0.367796	530.274	0.353631
535.796	0.962312	542.527	0.208498
546.531	0.258437	565.126	0.617049
565.36	0.693791	583.963	4.3128
576.196	3.19057	600.511	0.293416
602.362	0.360126	617.34	1.71058
616.62	2.88787	624.747	2.29508
624.712	2.35204	628.183	0.235028
648.654	0.335833	648.757	0.356486
651.92	0.271598	651.936	0.28474
659.982	0.0403487	660.01	0.0381813
675.741	0.10217	677.076	3.66055
677.306	3.96586	683.584	0.502034
709.872	1.69099	709.984	1.73634
721.729	1.81838	724.359	1.41636
735.589	0.478747	735.852	0.546769
739.209	0.41526	739.318	0.426755
742.643	0.502709	742.916	0.476511
748.176	0.0432437	749.403	0.15418
754.616	0.598939	754.356	1.23748
755.655	0.688663	755.561	0.234175
755.927	0.62963	756.056	0.520895
783.472	1.47108	783.396	1.57648
791.441	0.104467	791.964	0.0309826
793.789	4.15137	795.179	3.94439
798.408	0.73242	800.686	1.46755
822.723	1.30485	822.909	1.19783
833.761	0.0249228	834.046	0.0361464
839.42	0.193881	834.875	0.60752
843.056	0.559092	839.806	0.120736
853.547	1.01733	844.22	0.575126
854.232	0.149548	854.551	0.179627
859.579	0.869533	859.998	0.652637
864.335	0.278478	864.714	0.744567
869.489	0.439061	869.561	0.84571
872.559	2.68508	872.717	2.86076
883.11	3.65356	883.566	3.63828
895.913	0.150637	890.586	0.00850053
901.19	0.110983	900.466	0.105201
904.09	2.19258	904.476	1.03419

---

---

904.204	0.69159	905.957	2.56167
935.762	1.26764	932.912	1.66935
938.779	0.0982385	938.672	0.127213
973.652	5.61879	959.14	9.13671
976.921	0.123225	977.197	0.190337
980.813	0.527909	981.397	1.76147
986.025	0.00424105	986.045	0.0203706
993.542	0.0417909	992.009	0.630275
999.17	0.0288861	993.747	0.0317484
1003.25	0.0116015	999.223	0.028346
1010.13	3.48683	1002.93	0.0216178
1012.5	0.0770333	1009.77	1.79667
1012.99	1.58117	1013.16	0.117115
1021.72	6.69011	1017.66	0.0483338
1025.3	4.69338	1020.82	7.61671
1028.9	0.0411927	1028.74	0.0251406
1029.77	8.85293	1029.7	10.5932
1033.81	4.2705	1033.62	6.81405
1035.71	4.35544	1034.07	3.57202
1042.72	0.485776	1039.89	3.13547
1044.91	1.02238	1042.73	0.175929
1052.66	4.36977	1052.63	2.79733
1054.42	18.2115	1054.61	16.9121
1065.71	0.0634662	1060.88	0.0517033
1069.7	0.522525	1069.39	0.402708
1073.46	3.60196	1072.64	0.00748309
1074.4	0.35471	1073.5	3.84613
1084.94	2.40128	1084.75	1.5376
1089.36	48.8441	1089.28	51.0109
1103.47	5.80831	1101.25	0.0442859
1115.58	10.8205	1121.21	15.6356
1128.08	5.94159	1127.97	2.28746
1129.27	33.5435	1131.61	31.9143
1136.65	0.631404	1136.55	0.584917
1142.71	6.63373	1143.36	6.24668
1142.86	5.89336	1143.71	3.77056
1143.81	0.356398	1147.86	6.43443
1149.77	13.8567	1149.56	0.525829
1150.6	1.75313	1162.03	3.18992
1157.37	0.868678	1162.08	3.92977
1167.05	21.4272	1178.83	7.95065
1187.42	3.97639	1181.47	48.9978
1189.54	99.9861	1188.97	26.1868
1191.77	9.68667	1189.54	68.9113
1196.45	0.483223	1191.84	2.00254
1196.53	0.323997	1196.51	0.282848
1207.73	17.6005	1208.17	16.1404
1208.72	0.845689	1208.39	1.0523
1216.59	34.2453	1217.78	33.5312
1232.82	0.799539	1225.73	26.8041
1233.07	28.7272	1231.56	1.04178
1238.48	75.6705	1238.46	76.4962
1247.37	0.533849	1246.73	1.51504
1256.4	0.156748	1255.97	0.361792
1261.7	2.50932	1262.33	0.306424
1264.71	1.92944	1264.65	1.08073
1280.36	100	1280.47	100
1287.31	1.05552	1287.19	0.0738682
1290.71	35.3075	1291.73	43.4826
1295.5	10.5544	1295.54	10.3468
1298.66	0.415302	1299.02	1.06931

---

---

1301.88	2.89944	1301.77	3.13711
1305.46	1.93871	1305.62	3.02241
1315.02	0.801099	1314.9	0.83571
1315.39	0.378671	1321.96	0.554744
1325.13	0.127146	1323.88	7.37664
1326.05	0.035424	1325.5	1.7446
1326.77	0.157271	1325.73	2.59476
1327.65	7.67199	1326.25	0.025239
1332.97	2.42559	1332.93	2.63294
1336.15	0.109349	1335.74	0.134553
1337.04	0.514887	1337.07	0.684364
1339.62	0.0229679	1339.62	0.0427871
1342.4	0.202502	1342.12	0.978075
1342.9	0.123193	1342.4	0.37492
1344.85	0.338771	1342.67	0.0594599
1345.22	2.06495	1347.23	1.10208
1347.26	0.628637	1349.32	1.07588
1352.57	11.9093	1353.02	12.8522
1358.33	1.24637	1358.18	0.992144
1362.75	0.355062	1367.65	0.551057
1385.14	3.59242	1385.06	0.710773
1397.32	0.239956	1392.15	1.59757
1397.84	0.162784	1397.45	0.217053
1406.65	0.126922	1404.21	0.12241
1410.95	0.293872	1410.99	0.104315
1412.43	0.481749	1412.69	0.610616
1415.85	1.07073	1415.52	0.875915
1417.21	0.317438	1417.35	0.161871
1418.1	0.126409	1423.43	1.2308
1431.95	2.85164	1432.25	3.0177
1432.8	1.85124	1432.88	1.96585
1444.51	0.810489	1443.01	0.850786
1459.77	0.490509	1459.72	0.514659
1460.35	0.298679	1460.4	0.345929
1477.86	0.050978	1478.18	0.725586
1487.99	0.033437	1484.29	0.434741
1488.15	0.53653	1487.85	0.0446797
1489.4	0.0554541	1489.8	0.00147693
1489.84	0.00916579	1490.33	0.00377437
1491.27	0.0425066	1491.16	0.0122311
1491.77	0.671474	1494.5	0.518707
1497.86	0.0840198	1497.79	0.04701
1497.91	0.180314	1499.39	0.148918
1500.29	0.621041	1501.14	0.749491
1501.12	0.746531	1505.21	0.197689
1505.36	0.170176	1505.98	0.8648
1508.34	0.0539692	1510.32	0.0356431
1514.2	0.670214	1513.99	0.575684
1516.81	1.07116	1518.18	1.20426
1523.2	3.85039	1523.21	3.9513
1528.66	0.565224	1527.37	0.681705
1536.39	7.48593	1536.54	7.59961
1550.04	7.60866	1550.09	7.79398
1559.27	6.97204	1559.3	6.94699
1600.3	0.876049	1600.33	0.945364
1613.28	0.667661	1613.34	0.709165
1626.3	0.310953	1626.36	0.318677
1647.47	28.3529	1647.5	29.1129
1651.65	18.6867	1651.65	19.1861
1656.14	4.68372	1656.12	4.61192
1758.22	31.4954	1756.09	32.66

---

---

1780.79	28.0931	1781.16	28.984
2983.85	3.64077	2984.55	2.94433
2997.31	0.200301	2997.37	0.0738244
2998.44	1.41901	2998.57	1.57174
3001.95	0.550653	3002.07	0.976117
3003.1	0.217319	3003.24	0.196541
3004.3	1.52962	3004.19	0.551025
3012.62	1.06698	3004.52	4.82489
3012.97	4.87885	3013.01	3.70578
3014.51	0.29541	3014.43	5.00252
3014.69	5.1966	3014.99	0.962124
3020.81	0.209895	3020.75	0.400641
3024.14	2.90354	3020.8	0.576526
3025.8	4.13561	3024.09	3.64249
3027.97	4.91843	3025.82	4.85821
3028.87	0.0650472	3029.05	0.0523269
3031.73	2.26244	3030.24	3.18975
3034.48	2.51305	3032.34	1.56355
3034.56	1.19851	3034.59	2.5957
3035.54	5.86719	3034.88	5.56337
3037.76	2.76151	3044.19	2.4791
3039.3	3.89438	3044.58	2.79592
3040.92	1.14362	3046.78	0.499759
3049.6	2.15721	3053.35	1.34525
3053.34	1.48056	3058.6	4.42615
3069.51	7.0687	3076.71	0.326346
3076.96	0.139282	3078.05	5.25754
3079.52	13.56	3079.1	1.68517
3083.67	7.30525	3079.37	14.3291
3086.02	1.02818	3083.34	8.94859
3088.69	1.49794	3088.9	4.89425
3088.74	4.02751	3110.01	3.03774
3109.05	4.96179	3113.53	1.04075
3112.63	2.41089	3118.4	3.12484
3182.75	1.01481	3182.77	1.15035
3183.56	1.25941	3183.64	1.16215
3187.97	0.225107	3187.94	0.265453
3189.85	0.480008	3190.04	0.513368
3196.44	0.518807	3196.35	0.523072
3201.41	0.0152763	3201.53	0.0116185
3202.75	0.530163	3202.9	0.452607
3208.11	0.383831	3207.63	0.411001
3217.31	0.224989	3216.32	0.22365
3219.19	0.2541	3219.29	0.267663
3220.42	0.539276	3219.56	0.549537
3221.82	1.04464	3222.27	1.1249

---



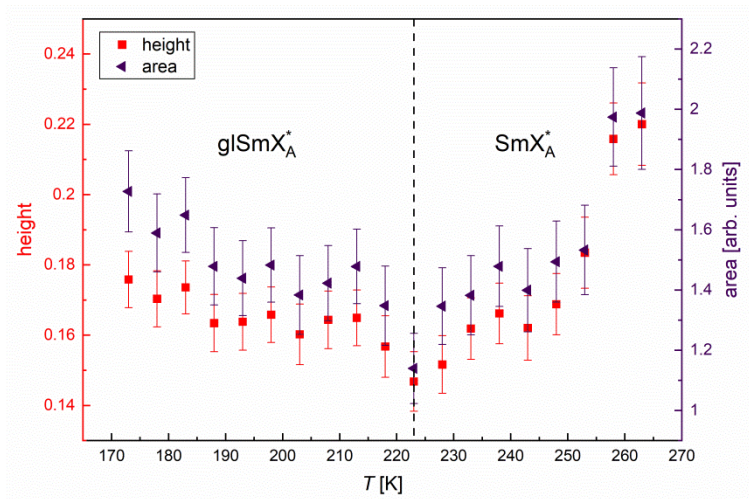


Figure S2. Height and area of the band IV in the  $\text{SmX}_A^*$  phase and its glass.

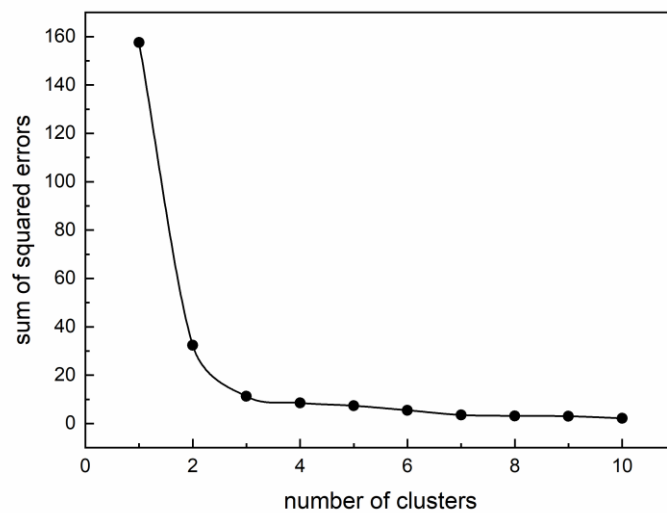


Figure S3. Application of the elbow method for the IR spectra of 7HH6 in the  $1650\text{-}1850\text{ cm}^{-1}$  range. The line connecting points is a guide to an eye.